Supporting Information

Coordination environments of platinum single atom catalysts from NMR fingerprints

Jonas Koppe[1], Alexander V. Yakimov[2], Domenico Gioffrè[2], Marc-Eduard Usteri[2], Thomas Vosegaard[3], Guido Pintacuda[1], Anne Lesage[1], Andrew J. Pell[1], Sharon Mitchell[2], Javier Pérez-Ramírez[2,*], Christophe Copéret[2,*]

[1]Centre de RMN Très Hauts Champs de Lyon (UMR5082 - CNRS, ENS Lyon, UCB Lyon 1), Université de Lyon, 5 rue de la Doua, Villeurbanne FR-69100, France

[2]Department of Chemistry and Applied Biosciences, ETH Zürich, Vladimir-Prelog-Weg 1, Zürich CH-8093, Switzerland

[3]Department of Chemistry and Interdisciplinary Nanoscience Center, Aarhus University, Gustav Wieds Vej 14, DK-8000 Aarhus C, Denmark

E-mail: jpr@chem.ethz.ch; ccoperet@ethz.ch

Table of Contents

1. Conventional characterization of supported samples

1.1 Elemental analysis (EA)

Mikroanalytisches Labor Pascher (An der Pulvermühle 1, 53424 Remagen - Bandorf, Germany) performed the Pt EA via Inductively coupled plasma atomic emission spectroscopy (ICP-AES). EA of other elements (H, C, N, Cl) were measured by the in-house EA service at ETHZ via IR spectrometry (H, C, N; LECO) or Schöniger digestion/IC (Cl).

Table S1: EA composition of the Pt@NC materials, and resulting Cl/Pt atomic ratios.

Material	Ann. step	C (wt%)	H (wt%)	N (wt%)	Cl (wt%)	Pt (wt%)	Cl/Pt ratio
Pt@NC-5	1	53.24	1.92	21.55	2.83	4.33	3.60
	2	56.98	1.58	22.84	1.48	5.15	1.58
Pt@NC-15	1	46.06	1.70	18.95	4.88	14.80	1.81
	2[#]	50.23	1.27	20.29	2.37	14.60	0.89
Pt@NC-15 (Pt@NC batch 2)	2	52.16	1.38	18.02	2.28	13.90	0.90

[#]In the Figure 4 in the main text also referred to as Pt@NC (batch 1)

1.2 HAADF-STEM

HAADF-STEM with EDX elemental mapping was performed for the Pt@NC-5 on a Talos F200X microscope to confirm the dispersity of N, Pt, and Cl across particles due to the microscope's high sensitivity detector. Furthermore, the Pt@NC-15 sample after both annealing steps, which is more likely to sinter, was analyzed on a high-resolution JEOL GrandARM microscope. Multiple regions were analyzed at different magnifications to confirm the isolation of Pt atoms.

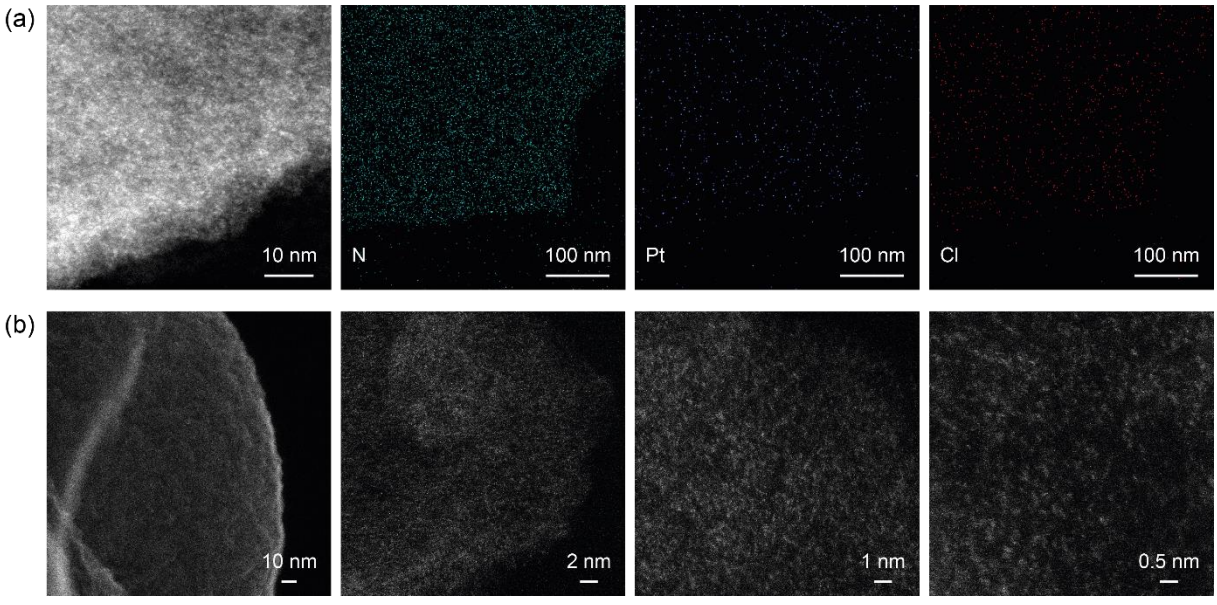

Figure S1. (a) HAADF-STEM images with EDX maps of Pt@NC-5 confirming the presence and dispersion of the elements of interest, (b) High-resolution micrographs of Pt@NC-15 after the second annealing step at different magnifications and sample regions, confirming atomic dispersion of Pt on the surface of NC.

1.3 X-Ray Photoelectron Spectroscopy

N 1s, Pt 4f, O 1s, and C 1s XPS spectra (**Figure S2**) were measured and fitted (**Tables S2** and **S3**) for the Pt@NC materials at different loadings (5 and 15 wt%) and synthesis stages (1st and 2nd annealing step) as well as the pure carrier prior to Pt introduction. Five N moieties were considered for the XPS fitting of the N1s spectra based on previous reports:[1,2] pyridinic N (N_1), pyrrolic N (N_2), oxidized N (N_4), metal-bound N and aminic N; the last two were grouped together into a single contribution N_3 to prevent overfitting due to insufficient separation of their chemical shifts.[1] The fitting shows an almost constant contribution of both N_2 and N_4, whereas an increase in N_3 at the cost of N_2 upon metal introduction and increase of the loading can be observed (**Table S2**). Accordingly, it may be inferred that Pt atoms preferably bind to pyridinic N moieties as conversion of pyridine N to aminic N seems unlikely. XPS spectra of the other elements show no changes upon metal introduction and increase of the loading. Accordingly, binding with carbon or oxygen, if present, is almost negligible. Fitting of the Pt 4s spectra based on various nitrogen and chlorine-containing molecular compounds shows that the Pt is present in a +II oxidation state, consistent with both XAS and NMR. Further changes could not be quantified. Cl could not be analyzed due to a combination of low loading and scan rates.

Table S2. XPS data of N 1s spectra of the different Pt@NC samples as well as the Pt-free carrier.

Sample	Pyridinic-N[a]			Pyrrolic-N[a]			N-M/N-H[a]			N-O[a]		
	Position / eV	FWHM[b] / eV	Area / %	Position / eV	FWHM / eV	Area / %	Position / eV	FWHM / eV	Area / %	Position / eV	FWHM / eV	Area / %
NC	398.2	1.53	47.09	400.1	2.10	40.46	399.1	1.65	7.21	403.5	2.50	5.24
Pt@NC-5-1	398.1	1.42	41.12	400.1	1.95	38.23	399.2	1.59	15.63	403.3	2.50	5.02
Pt@NC-5-2	398.1	1.39	38.84	400.2	2.22	38.71	399.1	1.64	15.99	403.5	2.50	6.46
Pt@NC-15-1	398.1	1.51	35.41	400.2	2.12	39.52	399.1	1.51	20.06	403.5	2.50	5.01
Pt@NC-15-2	398.1	1.32	34.11	400.3	2.20	36.97	399.1	1.44	24.08	403.5	2.50	4.84
Pt@NC-15-2[c]	398.2	1.28	30.93	400.4	2.22	37.59	399.1	1.50	26.8	403.5	2.50	4.68

[a]Assigned based on reference values[1,2] [b]FWHM: full width at half maximum [c]batch 2

Table S3. XPS fitting data for the Pt 4f spectra of the different Pt@NC samples.

Sample	Pt(IV)[a]			Pt(II)[a]			Pt(0)[a]		
	Position / eV	FWHM / eV	Area / %	Position / eV	FWHM / eV	Area / %	Position / eV	FWHM / eV	Area / %
Pt@NC-5-1	75.2	1.85	0	72.5	1.60	100	71.2	2.50	0
Pt@NC-5-2	75.5	2.50	0	72.7	1.49	100	71.2	2.48	0
Pt@NC-15-1	75.3	2.50	0	72.5	1.67	100	71.0	2.44	0
Pt@NC-15-2	75.1	2.50	0	72.6	1.64	100	71.2	2.48	0
Pt@NC-15-2[b]	75.4	2.32	0	72.7	1.50	100	71.3	2.48	0

[a]Assigned based on reference values[3] [b]batch 2

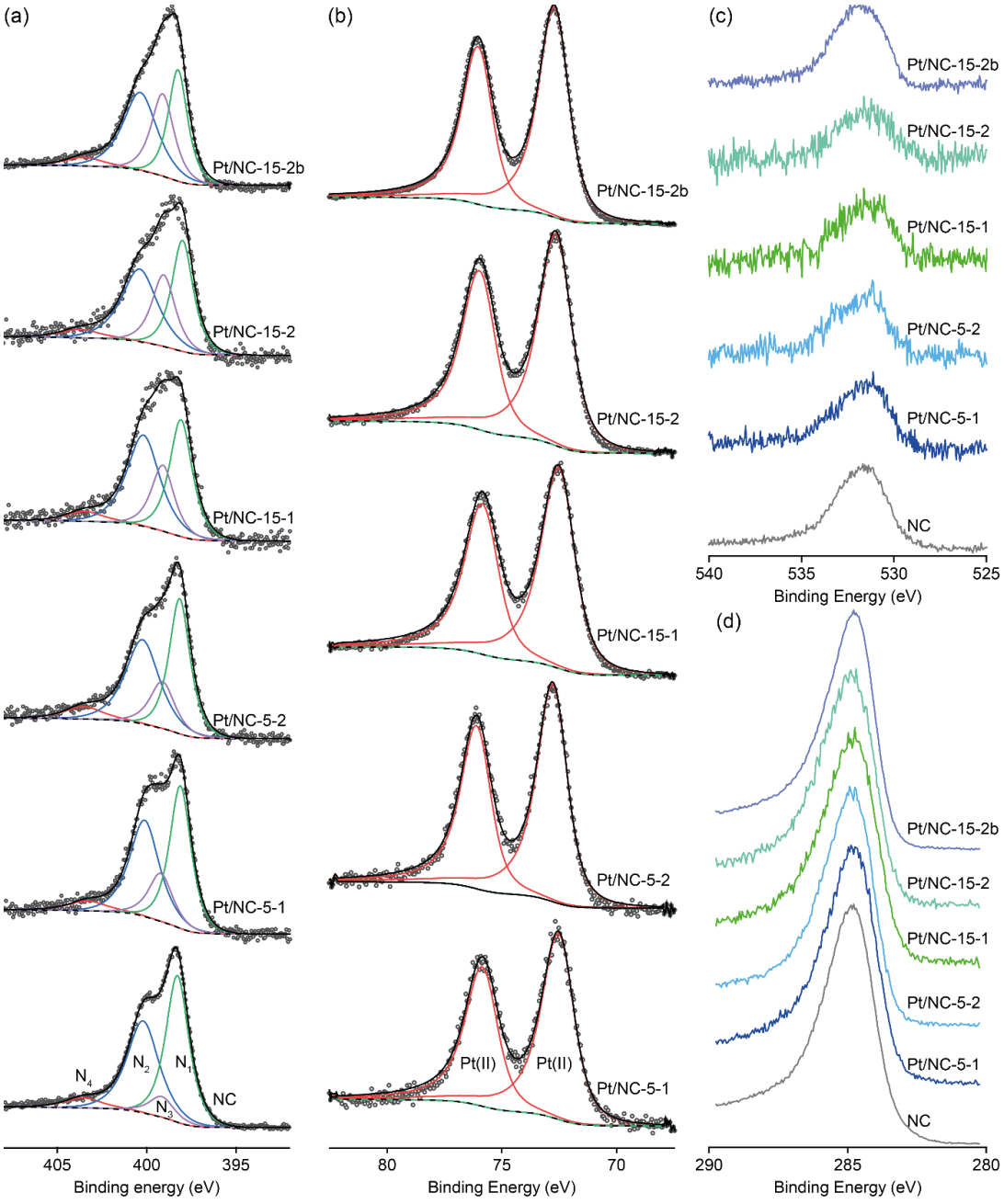

Figure S2. X-Ray Photoelectron Spectroscopy data for the Pt@NC samples studied in this work: N 1s with fitting (a), Pt 4f with fitting (b), O 1s (c), C 1s (d). In the fitted signal, the background is shown as a dashed line, the raw signals as circles, and the envelope as solid black lines. Code for (a): N_1: pyridinic N; N_2: pyrrolic N; N_3: metal-bound or amine N; N_4: oxidized N. In (b), Pt(IV) and Pt(0) contributions do not differ from the background (**Table S3**).

1.4 X-Ray Absorption Spectroscopy

X-Ray absorption spectroscopy (XAS) experiments were performed at BM31 of the Swiss-Norwegian Beamlines (SNBL) located at the European Synchrotron Radiation Facility (ESRF) in Grenoble, France. Pt L3 edge were collected in transmission mode using a double crystal Si (111) monochromator, a secondary reference (Pt-foil) was used for energy calibration (11564 eV). Typical beam dimensions used were 0.4 mm (H) x 4 mm (W). The sample was packed into quartz capillaries (1.5 mm W, 0.02 mm wall thickness). Spectra were collected at beam energies ranging from 11.46 to-12.36 keV. The scans (5 for molecular samples, 10 for materials) were averaged to obtain a sufficient quality for structural analysis. Demeter software (0.9.24) from the Ifeffit software package (Version 1.2.11) was used for the XAS data analysis.[4]

Pt L_3 edge XAS spectra of the Pt-foil (metallic) used as internal reference (11564 eV), a series of molecular complexes with varying Cl content in the 1st Pt coordination environment (K_2PtCl_4, *cis*-$Pt(py)_2Cl_2$, $Pt(NH_3)_4Cl_2$) and the Pt@NC materials with different Pt loadings (5wt%, 15wt%), annealed once and twice, are shown in **Figure S3.** XAS Pt L_3 edge spectra (a) and their 1st derivative spectra (b) of Pt-foil (metallic), $Pt(NH_3)_4Cl_2$, *cis*-$Pt(py)_2Cl_2$, K_2PtCl_4 and of the Pt@NC materials. The white line edge energy position (obtained as the highest point of the 1st derivative of the XAS spectra) spans between 11564 and 11566 eV. An increase of 1 eV is observed in the complex with a full-N 1st coordination environment vs. the Cl-containing complexes (comparison between $Pt(NH_3)_4Cl_2$, *cis*-$Pt(py)_2Cl_2$, and K_2PtCl_4). The Pt@NC samples have edge energies between 11565 and 11566 eV, consistent with Pt(II) oxidation state (**Table S4**). The comparison of the couples of materials with the same Pt loading after one or two annealing steps shows an increase in the white line intensity upon a second annealing step, in agreement with the dichlorination of the sample (see EA, **Section S1.1**), consistently to what was observed for the molecular samples. Interestingly, Pt@NC-5 2nd annealing and Pt@NC-15 1st annealing have a similar edge energy, consistent with a comparable Cl/Pt ratio found in the EA (**Section S1.1**).

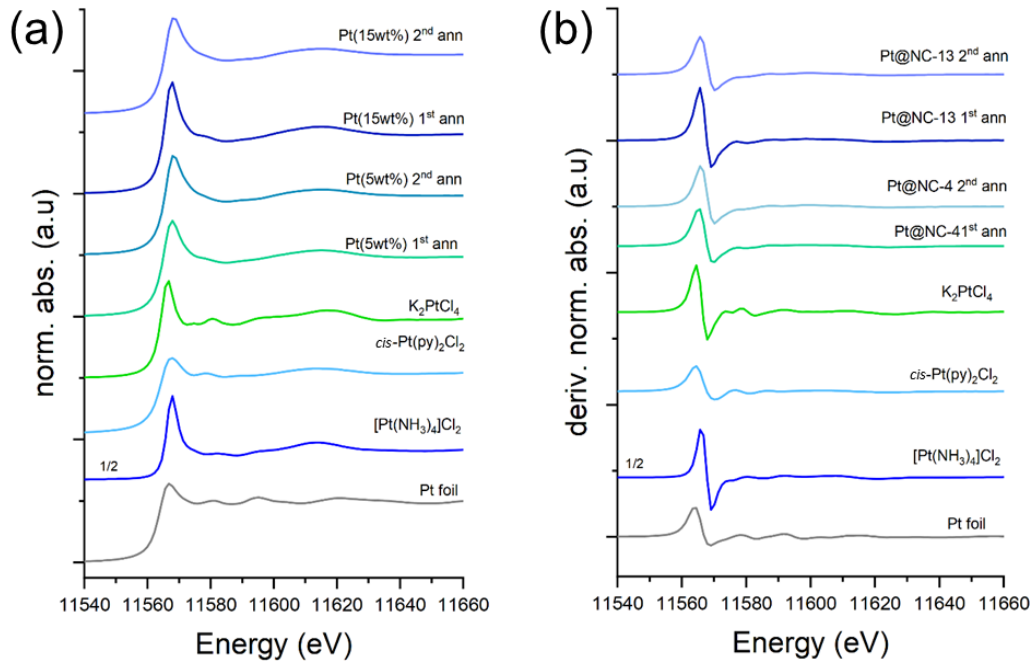

Figure S3. XAS Pt L_3 edge spectra (a) and their 1st derivative spectra (b) of Pt-foil (metallic), $Pt(NH_3)_4Cl_2$, *cis*-$Pt(py)_2Cl_2$, K_2PtCl_4, and of the Pt@NC materials.

Table S4: EXAFS Pt L_3 edge energies (eV) at the highest point of each 1st derivative spectrum, as well as distances (Å) at maximum intensity in R-space.

Material	Pt L_3 Edge Energy (eV)	Distance at highest intensity in R-space (Å)
Pt foil (metallic)	11564	2.61
K_2PtCl_4	11564	1.90
cis-Pt(tpy)$_2$Cl$_2$	11564	1.84
Pt(NH$_3$)$_4$Cl$_2$	11565	1.62
Pt@NC-5 1st ann	11565	1.66
Pt@NC-5 2nd ann	11566	1.56
Pt@NC-15 1st ann	11566	1.66
Pt@NC-15 2nd ann	11566	1.53

EXAFS spectra are shown in **Figure S4** for (a) k-space and (b) R-space. EXAFS spectra (k-weight = 3, k-space window (Å^{-1}): 3-12 (Pt foil); 3-8 (others)) suggest the absence of metallic Pt (absence of Pt-Pt path, 2.61 Å) for both the molecular samples and the Pt@NC series of materials, in agreement with the presence of isolated Pt sites. A comparison of the materials with the same Pt loadings shows a shift in the distance with highest intensity upon annealing: Pt@NC-5 (1.66 to 1.56 Å) and Pt@NC-15 (1.66 to 1.53 Å). This is consistent with the trend observed among the three molecular complexes, for which maxima in the distance are found to be at 1.90 Å (K_2PtCl_4), 1.84 Å (*cis*-Pt(py)$_2$Cl$_2$), and 1.62 Å (Pt(NH$_3$)$_4$Cl$_2$), going from 4 to 0 Cl atoms in the 1st coordination shell of Pt (**Table S4**). The decrease in intensity of the Pt-Cl path (1.90 Å) and an increase in the Pt-N path (1.62 Å) upon a second annealing step is therefore consistent with the de-chlorination of the samples, and changes in the 1st coordination environment of Pt upon annealing (**Figure S4**).

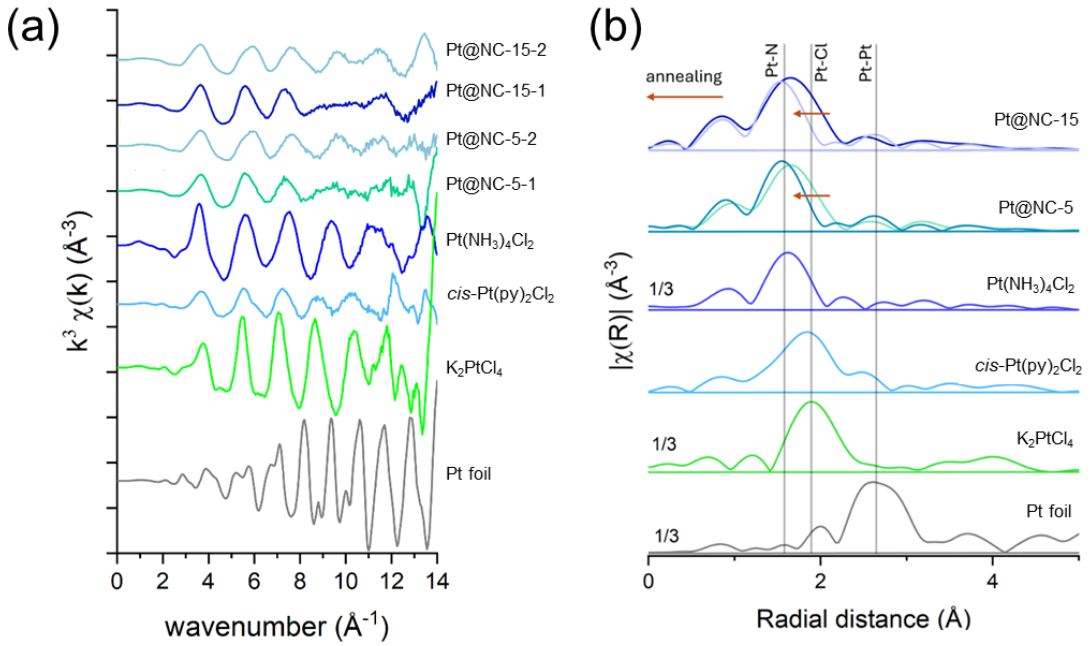

Figure S4. EXAFS Pt L_3 edge spectra of Pt-foil (metallic), Pt(NH$_3$)$_4$Cl$_2$, *cis*-Pt(py)$_2$Cl$_2$, K_2PtCl_4, and of the Pt@CN materials: (a) k-space and (b) R-space. In (b), vertical lines indicate distances (Å) of: 2.61 (Pt-Pt); 1.90 (Pt-Cl); 1.62 (Pt-N).

2. Experimental ^{195}Pt NMR parameters

^{195}Pt NMR spectra have been recorded using the WCPMG pulse sequence under static and MAS conditions shown in **Figure S5**.[5,6]

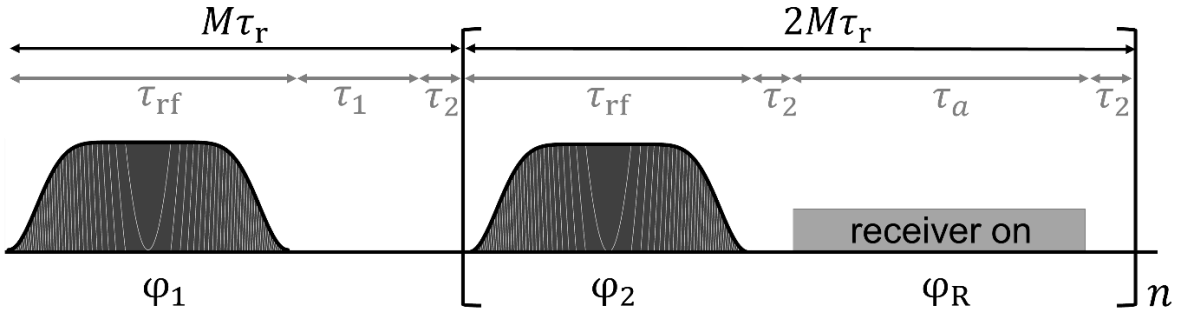

Figure S5. WCPMG NMR pulse sequence for static and MAS conditions. Identical WURST-N pulses of length τ_{rf} are used, and the acquisition time is denoted as τ_a. A short ringdown delay τ_2 can be incorporated to reduce pulse artifacts. The number of CPMG echoes is given by *n*. The pulse phases are set according to $\phi_1 = \phi_2 - \frac{\pi}{2} = \phi_R$, where ϕ_R represents the receiver phase. The first echo delay is set to $\tau_1 = (\tau_a - \tau_{rf})/2$.[7] Under MAS conditions, the sequence is synchronized with the rotation, where τ_r denotes the rotation period.[6] Then, the first echo delay must be set to $\tau_1 = M\tau_r - \tau_{rf}$, where *M* is an integer number, defining the number of rotor echoes recorded with each echo in the CPMG train. Rotor synchronization is ensured by setting the acquisition time to $\tau_a = 2M\tau_r - \tau_{rf} - 2\tau_2$. A minimum phase cycle should be employed for optimum S/N.[7]

The ^{195}Pt NMR measurements (static and 20 kHz MAS) on the molecular compounds K_2PtCl_4, *cis*-$Ptpy_2Cl_2$, $Pt(NH_3)_4Cl_2$, and *cis*-$PtMe_2$tmeda were conducted at room temperature in a single offset using *continuous-wave* ^{1}H decoupling (20 kHz). For K_2PtCl_4, two offsets were required (spaced by 250 kHz), and no ^{1}H decoupling was applied. The experimental parameters are again summarized in **Table S5** and **Table S6**.

The ^{195}Pt NMR measurements (static and 10 kHz MAS) on the samples containing single Pt atoms were conducted at low temperature (100 K) using two offset (spaced by 250 kHz). The spectrum of Pt@PTI was recorded at a single offset only. The experimental parameters are again summarized in **Table S7** and **Table S8**.

All ^{195}Pt NMR spectra were obtained by coadding the individual echoes of the WCPMG-echo train in the time domain prior to Fourier transform and magnitude calculation. The resulting full echoes were apodised using a Hamming window function[8] with $\alpha = 0.54$ (cf. **Figure S7**). This is illustrated in **Figure S6**.

When the full ^{195}Pt NMR signatures were reconstructed from two subspectra, the skyline projection method was used. For the sample Pt@NC-15 (1st. annealing), the second subspectrum (static and MAS) needed to be recorded with a freshly packed rotor, due to a rotor crash at the end of the acquisition of the first subspectrum. To compensate for the difference in sample volume, the intensities for both subspectra were scaled to match at the center in between their frequency offsets (cf. **Figure S11**). This resulted in a down-scaling of the second subspectrum (static and MAS) by 10 %.

We note that in the ^{195}Pt MAS NMR signals of the Pt@NC samples, no rotor echoes were observed due to the Pt-site heterogeneity, and ultimately large distribution of ^{195}Pt isotropic chemical shifts. Therefore, the full echo (after coadding all individual echoes from WCPMG train) was drastically apodised to reduce the noise. The full procedure is demonstrated in **Figure S7**.

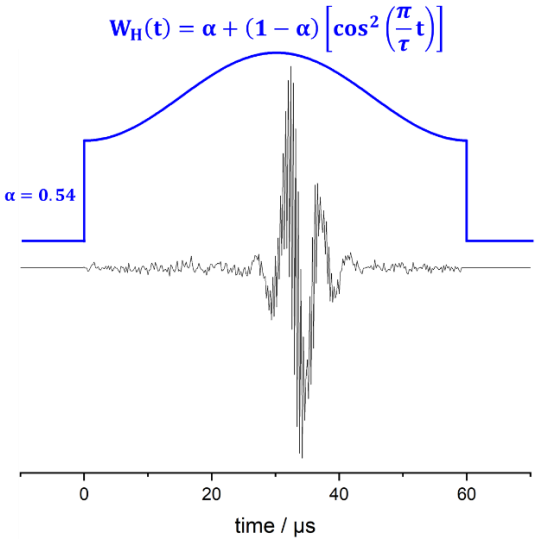

Figure S6. Illustration of the Hamming window function $W_H(t)$ used to process the coadded full echoes obtained from the WCPMG train. Here, τ is the window length and is set to match the full echo length (60 µs in this example). The truncation parameter α was set to $\alpha = 0.54$, offering a good compromise between the obtained linewidth and the signal-to-noise.[8]

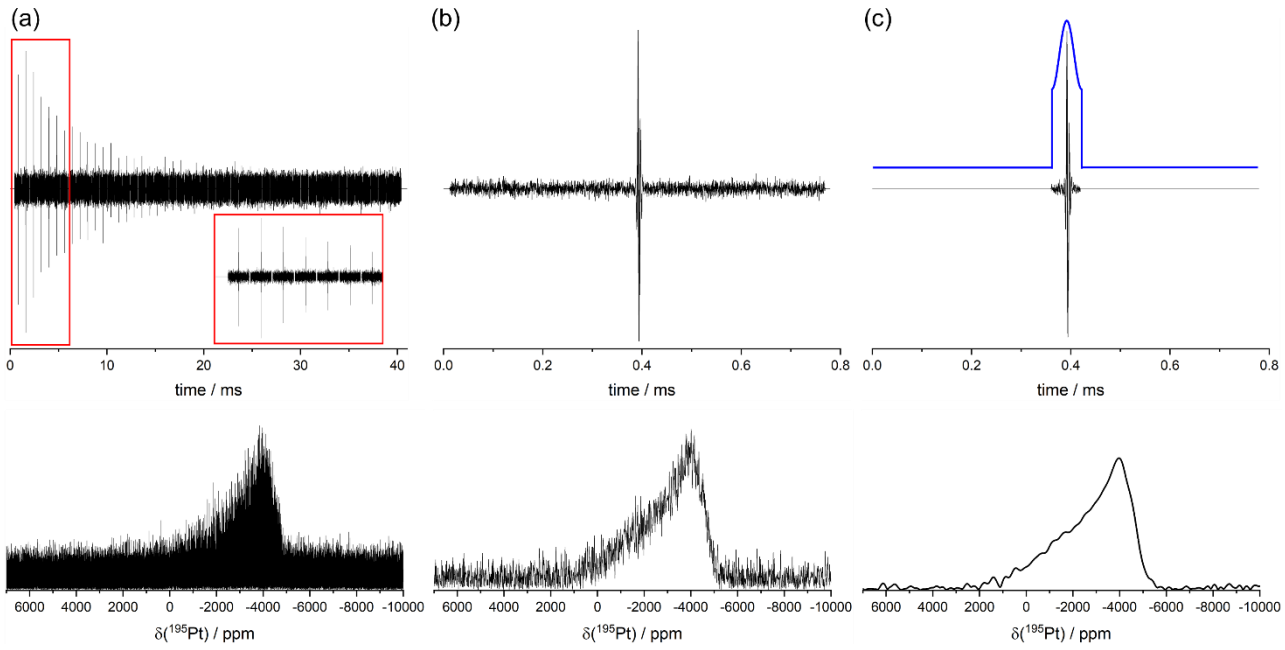

Figure S7. Processing procedure for WCPMG-MAS spectra. (a) Raw time-domain signal, i.e., the full WCPMG train with 50 echoes of length 730 µs, theoretically comprising 7 rotor echoes each (three rotor echoes for the built-up part, the central echo, and three rotor echoes in the decaying part). The bottom panel shows the corresponding frequency-domain spectrum obtained after FT of the full FID. (b) The full echo obtained from coadding the first 30 echoes from the WCPMG train in (a). Clearly, no rotor echoes are observed, such that most of the echo contains only noise, as can also be seen from the corresponding spectrum in the bottom panel. (c) Echo from (b), apodised to match the echo length used in the static WCPMG experiments (60 µs), combined with the Hamming window function in blue. The bottom panel shows the final ^{195}Pt WCPMG-MAS spectrum as reported in the main text. The exemplified data here correspond to the high Pt-loading samples Pt@NC (batch 2, **Figure 4**b in the main text).

Table S5. Static ^{195}Pt WCPMG NMR experiments on the molecular compounds in **Figure 2a-d**. The four numbers in a single line refer to the individual compounds in the following order: K_2PtCl_4, cis-$Ptpy_2Cl_2$, $Pt(NH_3)_4Cl_2$, and cis-$PtMe_2$tmeda.

Larmor frequency (MHz)	86.1183
Recycle delay (s)	30, 30, 4, 30
Dwell time (μs)	0.2
Processed echoes	200, 100, 75, 10
Number of scans[&]	1880, 5200, 4096, 2240
Echo delay τ_1 (μs)	60
Ring-down delay τ_2 (μs)	10
WURST-pulse length (μs)	30
Sweep width (kHz)	1400
WURST-pulse shape parameter, N	10
Nutation frequency[#] (kHz)	57

[&]Some experiments have larger number of scans than required due to overnight runtimes
[#]The ^{195}Pt nutation frequency was calibrated using K_2PtCl_6.

Table S6. ^{195}Pt WCPMG-MAS NMR (20 kHz) experiments on the molecular compounds in **Figure 2a-d**. The four numbers in a single line refer to the individual compounds in the following order: K_2PtCl_4, cis-$Ptpy_2Cl_2$, $Pt(NH_3)_4Cl_2$, and cis-$PtMe_2$tmeda.

Larmor frequency (MHz)	86.1183
Recycle delay (s)	30, 30, 4, 30
Dwell time (μs)	0.2
Processed echoes	100, 100, 75, 10
Number of rotor echoes	5
Number of scans[&]	48, 1888, 15360, 216
Echo delay τ_1 (μs)	230
Ring-down delay τ_2 (μs)	10
WURST-pulse length (μs)	50
Sweep width (kHz)	3000
WURST-pulse shape parameter, N	2
Nutation frequency[#] (kHz)	65

[&]Some experiments have larger number of scans than required due to overnight runtimes
[#]The ^{195}Pt nutation frequency was calibrated using K_2PtCl_6.

Table S7. Static ^{195}Pt WCPMG NMR experiments on the sample containing single Pt atoms **Figure 2e-h**., and **Figure 4.** The six numbers in a single line refer to the individual samples in the following order: Pt@NC-4 first and second annealing, Pt@NC-13 first and second annealing, Pt@NC (batch 2), Pt@PTI.

Larmor frequency (MHz)	86.1183
Recycle delay (s)	0.2
Dwell time (μs)	0.2
Processed echoes	100
Number of scans[&]	1303632, 225536, 47672, 37520, 368967, 404744
Echo delay τ_1 (μs)	60
Ring-down delay τ_2 (μs)	10
WURST-pulse length (μs)	30
Sweep width (kHz)	1400
WURST-pulse shape parameter, N	10
Nutation frequency[#] (kHz)	57

[&]Some experiments have larger number of scans than required due to overnight runtimes

[#]The ^{195}Pt nutation frequency was calibrated using K_2PtCl_6.

Table S8. ^{195}Pt WCPMG-MAS NMR (10 kHz) experiments on the sample containing single Pt atoms **Figure 2e-h**. The four numbers in a single line refer to the individual samples in the following order: Pt@NC-4 first and second annealing, Pt@NC-13 first and second annealing.

Larmor frequency (MHz)	86.1183
Recycle delay (s)	0.2
Dwell time (μs)	0.2
Processed echoes	20, 40, 50, 50
Number of rotor echoes	3
Number of scans[&]	833696, 385496, 66952, 65536
Echo delay τ_1 (μs)	230
Ring-down delay τ_2 (μs)	10
WURST-pulse length (μs)	50
Sweep width (kHz)	3000
WURST-pulse shape parameter, N	2
Nutation frequency[#] (kHz)	65

[&]Some experiments have larger number of scans than required due to overnight runtimes

[#]The ^{195}Pt nutation frequency was calibrated using K_2PtCl_6.

3. Additional ^{195}Pt NMR data

Notably, direct detection via ^{195}Pt WCPMG NMR of single Pt atoms without any further, more advanced sensitivity-enhancement protocols (e.g., dynamic nuclear polarization) is enabled by the combined effects of low experimental temperatures (100 K) and very fast repetition rates (0.2 s). While this combination has already been exploited by Slichter and co-workers in their pioneer work on *metallic* Pt,[9–12] such short longitudinal relaxation (T_1) times are atypical for Pt(II). The longitudinal relaxation behavior and the effect of the temperature on the ^{195}Pt NMR lineshape for Pt@NC is demonstrated for the example of the high Pt-loading sample Pt@NC (batch 2; from **Figure 4**b of the main text) in **Figure S8**.

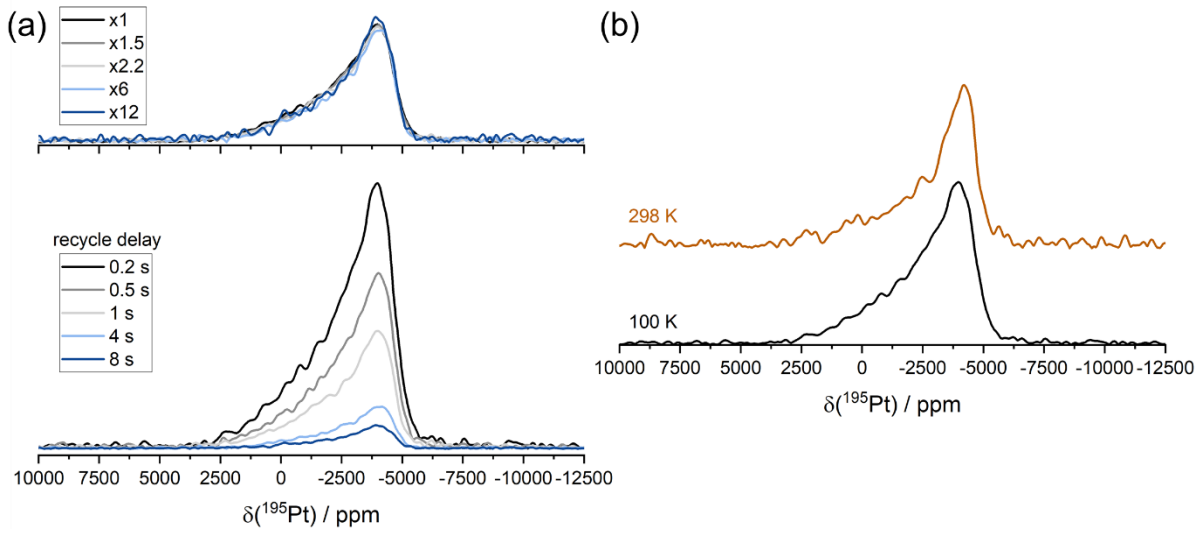

Figure S8. Effect of the recycle delay at 100 K (a) and the temperature at a recycle delay of 0.2 s (b) on the static ^{195}Pt NMR signature of Pt@NC (batch 2). Only the first subspectrum (first offset) is shown.

Neither the short repetition rates nor the low temperatures do impact significantly on the lineshape. Generally, low temperatures may have a deleterious effect on the ^{195}Pt T_1 relaxation times of molecular Pt(II) compounds, which in many cases even at room temperature exhibit unfavorable T_1 relaxation times (30 s and more). However, we suspect that due to the (partial) integration of the Pt centers into the surface of the support material, the surface dynamics, modulating the large shift anisotropies, cause efficient ^{195}Pt spin-lattice relaxation even at low temperatures. This is further corroborated by the fact that the Pt@NC sample with the (presumably) least degree of Pt surface integration (Pt@NC-5, first annealing) required the longest experimental times (1.5 days per subspectrum), while samples with equivalent Pt-loading (Pt@NC-5, second annealing) or even less (Pt@PTI, 2 wt%) but a (presumably) better Pt surface integration could be recorded in significantly shorter times (less than one day).

We also tested the effect of CPMG acquisition on the ^{195}Pt NMR spectra. Again, we found that the lineshape integrity is fully maintained, as demonstrated in **Figure S9**.

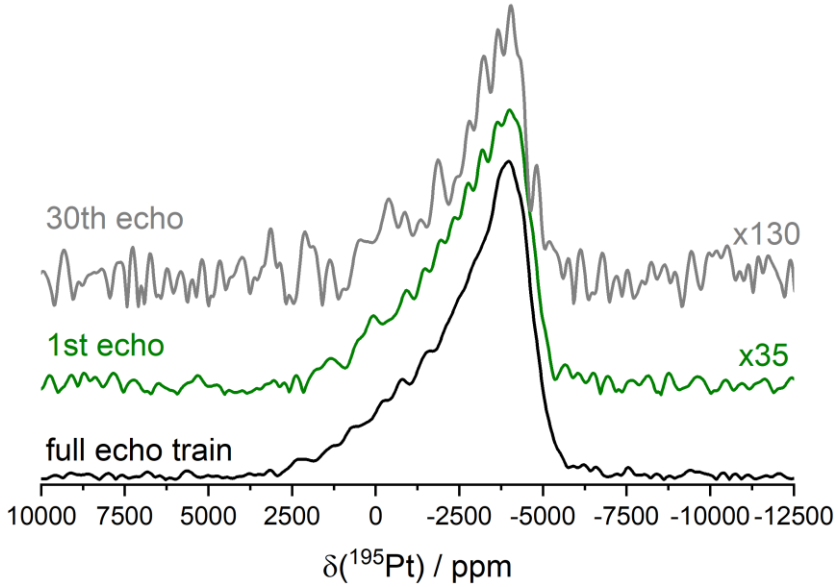

Figure S9. Effect of the CPMG acquisition on the static ^{195}Pt NMR signature of Pt@NC (batch 2). Spectra resulting from FT and magnitude calculation of the echo obtained from adding up 100 WCPMG echoes (full echo train), as well as the first and 30th echo only are compared.

As it was discussed in the main text, the Pt-site heterogeneity causes a Gaussian distribution of ^{195}Pt isotropic chemical shifts much larger than the applied MAS frequency (10 kHz). Therefore, we evaluated the effect of fast spinning (50 kHz MAS) on the lineshape for the high Pt-loading sample Pt@NC (batch 2, as already shown above). The ^{195}Pt WCPMG MAS spectrum (50 kHz MAS; first subspectrum) is shown in **Figure S10**.

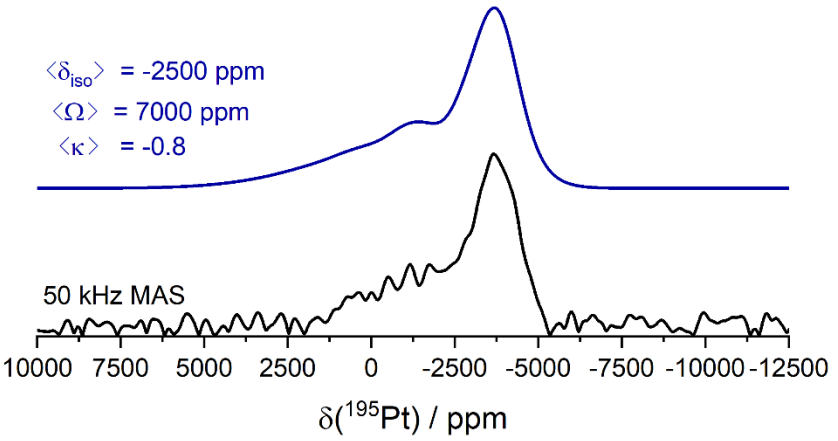

Figure S10. ^{195}Pt MAS NMR spectrum of Pt@NC (batch 2) at 50 kHz MAS (first subspectrum). The model (blue line) was obtained based on the parameters used to compute the static lineshape shown in **Figure 4b** in the main text.

Based on the Monte-Carlo simulation of the static lineshape shown in **Figure 4b** in the main text, we expect a standard deviation of ^{195}Pt isotropic chemical shift of 760 ppm, at the order of the MAS frequency (50 kHz ≈ 600 ppm). The spectrum indeed appears to show slight narrowing, and the experimental and numerical data are in close agreement, further supporting the lineshape model developed in this study.

Lastly, we show the effect of including a second offset (a second subspectrum) in the re-construction of the overall ^{195}Pt NMR signatures of the samples containing single Pt atoms. This is demonstrated for the sample Pt@NC-4 (first annealing; **Figure 2**e in the main text), showing the largest extension towards

higher frequencies (towards the left) of all samples. As a reference, the frequency axis (in MHz) is likewise indicated. The carriers (subspectrum centers) are demonstrated by the arrows.

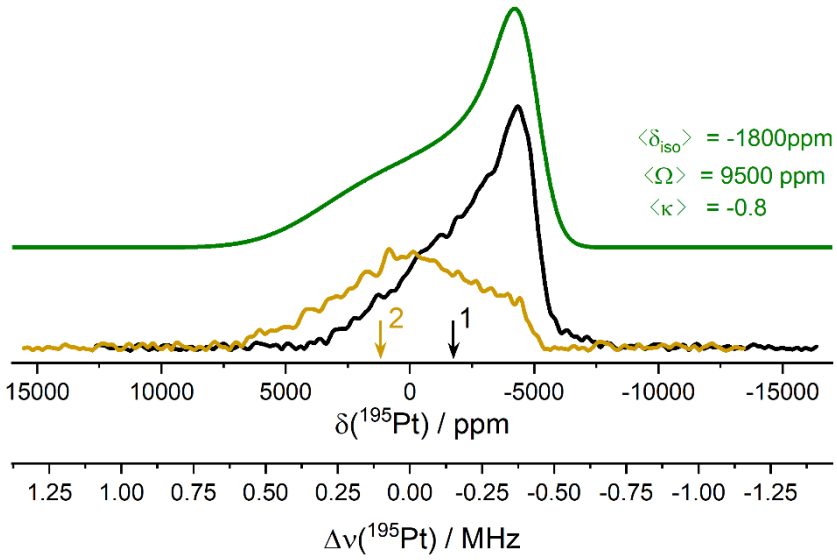

Figure S11. Effect of including a second subspectrum in the re-construction of the overall static ^{195}Pt NMR signature of Pt@NC-4 (first annealing).

4. DFT computations

Geometry optimization of a series of Pt(II) model complexes and calculations of their ^{195}Pt NMR spectroscopic parameters were performed using ADF 2022 with the hybrid PBE0 functional and Slater-type basis sets of quadruple-ζ quality (QZ4P) for Pt, triple-ζ quality (TZP) for the Pt first coordination shell and double-ζ quality (DZP) for other atoms[13]. Relativistic effects were treated by the two-component zeroth order regular approximation (ZORA)[14–16].

4.1 Benchmarking

^{195}Pt NMR computations have been benchmarked using a library of seven molecular Pt(II) square-planar complexes with δ_{iso} ranging between -360 and -3840 ppm and Ω going from 4600 up to 12521 ppm (**Table S9**). The calculated shielding values of the benchmark structures yielded good agreement (linear relationship) with the experimental chemical shift values (**Figure S12**); a good agreement between the experimental and DFT Ω values is also found (**Figure S13**), coherent with previous reports.[17,18] The cartesian coordinates of the optimized structures are found as an *addendum*.

Table S9*:* Molecular complexes used to benchmark DFT calculations. Experimental NMR parameters were obtained in this work (*a*), or reported in our previous collaborative work[17] (*b*) and by Schurko and collaborators[19] (*c*).

Molecule	σ_{iso} (DFT)	δ_{iso} (experiment)	Ω (DFT)	Ω (experiment)
$Pt(acac)_2$	2384	-360	12200	12521[b]
K_2PtCl_4	3194	-1650[a]	10586	9080[a]
cis-$Pt(NH_3)_2Cl_2$	4307	-1825	7473	8975[c]
cis-$Pt(py)_2Cl_2$	3892	-2065[a]	6085	8500[a]
trans-$Pt(NH_3)_2Cl_2$	4120	-2200	8770	9100[c]
$[Pt(NH_3)_4]Cl_2$	4589	-2540[a]	7078	7220[a]
$(tmeda)PtMe_2$	5827	-3840[a]	4173	4600[a]

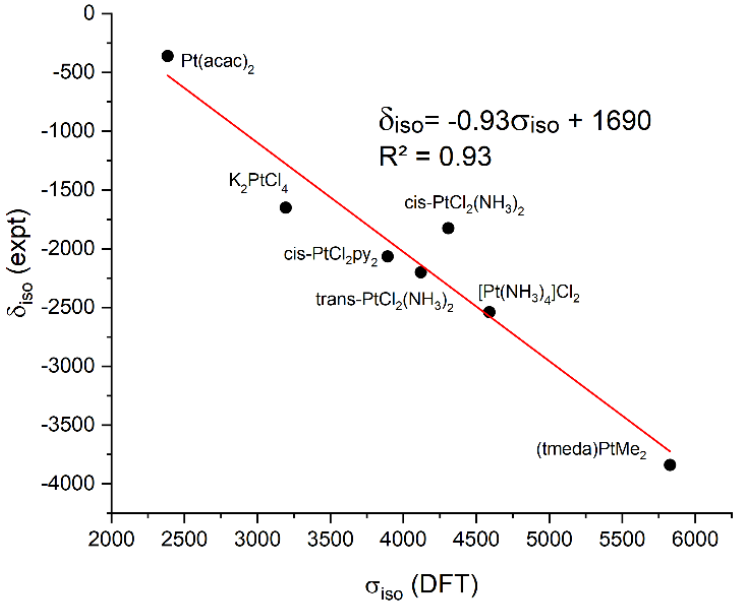

Figure S12. Correlation between experimental chemical shift $\delta_{iso}(^{195}Pt)$ and calculated chemical shielding $\sigma_{iso}(^{195}Pt)$ for a set of seven Pt(II) square-planar complexes. The linear relation is found to be δ_{iso}= -0.93 * σ_{iso} + 1690 ppm (R^2 = 0.93).

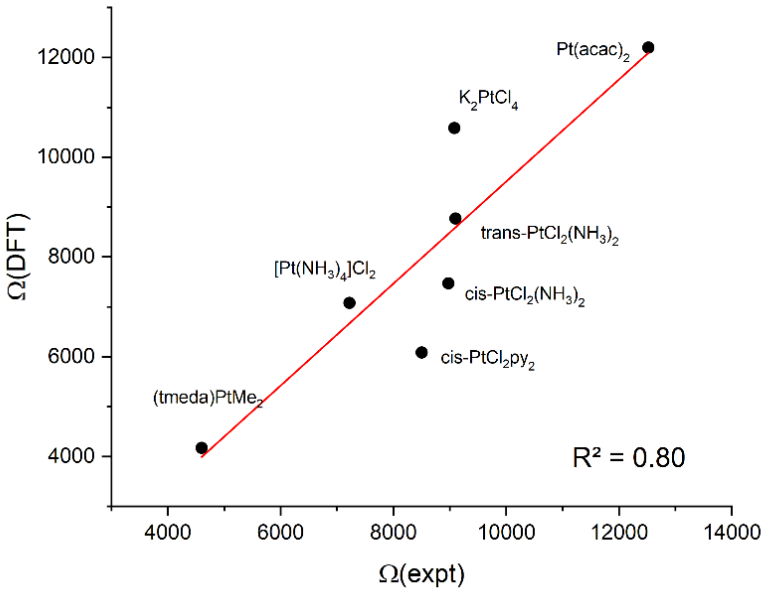

Figure S13. Correlation between experimental and calculated Ω values for a set of seven Pt(II) square-planar complexes.

4.2 DFT study on the effect of chemical environment on ^{195}Pt NMR parameters

We carried out a systematic study on the response of the ^{195}Pt NMR parameters (δ_{iso}, Ω) of a series of Pt(II) square-planar model complexes towards the Pt chemical environment (**Figure S14**, **Table S10**). The cartesian coordinates of the optimized structures are found as an *addendum*. δ_{iso} values were obtained referencing the computed σ_{iso} values *via* the obtained linear relationship:

$$\delta_{iso} = -0.93 * \sigma_{iso} + 1690\ ppm$$ (see **Section S4.1** for details)

Specifically, we considered a variety of ligands, coordinating the metal *via* O, C, N and C. We evaluated the effect of the different N and C ligands, including both aromatic (pyridine, pyrazine, benzene) and non-aromatic (ammonia, methyl) ones. The effects of chelating ligands (bipyridine, bipyrazine, biphenyl, tmeda) as well as that of possible isomers (*cis vs. trans*) were also taken into account. Overall, we found that the ^{195}Pt NMR parameters are related to specific coordination environments. The highest δ_{iso}/Ω are associated to a O_4 environment (-525/12200), both values decrease for Cl_4 environment (- 1278/9080). Further lower δ_{iso}/Ω values are observed in the series of N_2Cl_2 model compounds studied; these species cluster in the light-blue area of the δ_{iso}/Ω map (-1914 > δ_{iso} > -2353); 8770 > Ω > 4254), showing that the nature of the N-based ligands and of structural isomers can further modulate the NMR parameters. The family of N_4 structures (blue area) showed lower δ_{iso} values; the NMR parameters of these species appear to be only slightly sensitive to changes in the nature of the N-ligands (-2530 ppm > δ_{iso} > -2668 ppm; 7644 ppm > Ω > 6118 ppm). In contrast, the N_2C_2 species (grey area) show a large variability in δ_{iso} values (-2640 > δ_{iso} > -3941), while they all share relatively low Ω values (4278 > Ω > 2576). Similar trends have already been observed in previous studies.[17,18]

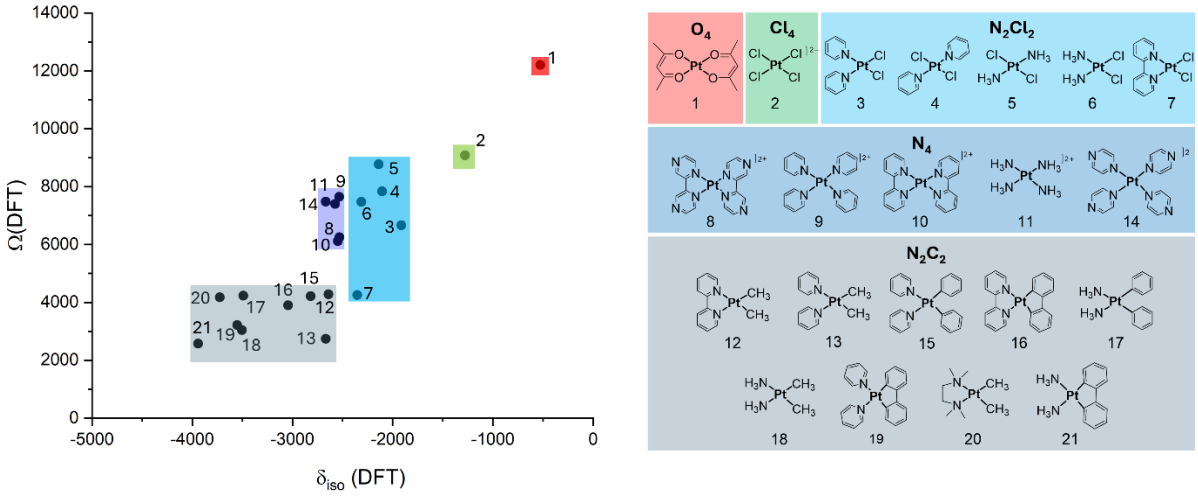

Figure S14. Ω *vs.* δ_{iso} map for the calculated Pt(II) square-planar model complexes (1-21). Compounds are couped according to their coordination environment to the Pt atom (O_4, red; Cl_4, green, N_2Cl_2, light blue; N_4, blue; N_2C_2, grey). Structures are numbered with respect to (ascending) δ_{iso} values.

Table S10: ^{195}Pt NMR parameters calculated for the **1**-**21** structures shown in **Figure S14**.

Structure	σ_{iso} (DFT)	δ_{iso} (DFT, referenced)	Ω (DFT)
1	2384	-525	12200
2	3194	-1278	9080
3	3878	-1914	6667
4	4083	-2104	7835
5	4120	-2138	8770
6	4308	-2313	7473
7	4351	-2353	4254
8	4542	-2530	6250
9	4543	-2532	7644
10	4558	-2546	6118
11	4589	-2575	7400
12	4659	-2640	4278
13	4688	-2667	2737
14	4690	-2668	7476
15	4850	-2817	4212
16	5093	-3043	3898
17	5574	-3490	4233
18	5589	-3504	3038
19	5641	-3552	3215
20	5827	-3725	4173
21	6059	-3941	2576

5. NMR lineshape model

5.1 General considerations

In the following, we indicate scalar deterministic variables as A, and random variables as A, where the superscript *(j)* is introduced, i.e., $A^{(j)}$, to identify an explicit event for the random variable A. The corresponding tensorial quantities are denoted as in $\mathbf{A}$, $\boldsymbol{A}$, and $\boldsymbol{A}^{(j)}$.
Under high-field conditions, the chemical shift (CS) tensor $\boldsymbol{\delta}$ can be described by a symmetric, second-rank Cartesian tensor within good approximation, and is therefore fully defined by six components,

$$\boldsymbol{\delta} = \begin{bmatrix} \delta_{11} & \delta_{12} & \delta_{13} \\ \delta_{12} & \delta_{22} & \delta_{23} \\ \delta_{13} & \delta_{23} & \delta_{33} \end{bmatrix}. \tag{1}$$

In principle, a random CS tensor $\widetilde{\boldsymbol{\delta}}$ can thus be construct from six random variables.[20] For the distribution of j ^{195}Pt sites, the corresponding ^{195}Pt NMR signatures can be described by the sum of individual NMR signals due to all CS tensors $\boldsymbol{\delta}^{(j)}$. For the model employed here, we assume that each $\boldsymbol{\delta}^{(j)}$ comprises two contributions, and can be expressed as

$$\boldsymbol{\delta}^{(j)} = \boldsymbol{\delta}^{\mathbf{0}} + \widetilde{\boldsymbol{\delta}}^{(j)} = \begin{bmatrix} \langle\delta_{11}\rangle & 0 & 0 \\ 0 & \langle\delta_{22}\rangle & 0 \\ 0 & 0 & \langle\delta_{33}\rangle \end{bmatrix} + \begin{bmatrix} \Delta\delta_{11}^{(j)} & \Delta\delta_{12}^{(j)} & \Delta\delta_{13}^{(j)} \\ \Delta\delta_{12}^{(j)} & \Delta\delta_{22}^{(j)} & \Delta\delta_{23}^{(j)} \\ \Delta\delta_{13}^{(j)} & \Delta\delta_{23}^{(j)} & \Delta\delta_{33}^{(j)} \end{bmatrix}, \tag{2}$$

implying that that $\boldsymbol{\delta}^{(j)}$ is described in a frame of reference where $\boldsymbol{\delta}^{\mathbf{0}}$ is diagonal. We note the close resemblance to the extended Czjzek model[20,21] (see discussion below), where $\boldsymbol{\delta}^{\mathbf{0}}$ is referred to as the local contribution that is identical for all sites, and $\widetilde{\boldsymbol{\delta}}^{(j)}$ (apart from the scaling factor, see Eq. (9)[20,21]) was termed the noise or background contribution, that varies across the different local environments. Within the model introduced in this study, $\boldsymbol{\delta}^{\mathbf{0}}$ contains information about the average or dominant local Pt(II) environment (in the later analysis determining the peak center in δ_{iso}-Ω-space), while $\widetilde{\boldsymbol{\delta}}^{(j)}$ comprise information about Pt(II)-site heterogeneity (the peak width and extension in δ_{iso}-Ω-space). To simplify the model in Eq. (2) and to reflect the close to axially symmetric (oblate) of square-planar Pt(II) sites, we approximate $\boldsymbol{\delta}^{(j)}$ by

$$\boldsymbol{\delta}_{\boldsymbol{sq}}^{(j)} = \begin{bmatrix} \langle\delta_{11}\rangle & 0 & 0 \\ 0 & \langle\delta_{22}\rangle & 0 \\ 0 & 0 & \langle\delta_{33}\rangle \end{bmatrix} + \begin{bmatrix} U_{\mathrm{long}}^{(j)} & 0 & 0 \\ 0 & U_{\mathrm{eq}}^{(j)} & 0 \\ 0 & 0 & U_{\mathrm{eq}}^{(j)} \end{bmatrix}, \tag{3}$$

where $\langle\delta_{11}\rangle \geq \langle\delta_{22}\rangle \geq \langle\delta_{33}\rangle$, and $U_{\mathrm{long}}^{(\mathrm{j})}$ and $U_{\mathrm{eq}}^{(j)}$ are treated as independent random variables, described by Gaussian distributions $U_{\mathrm{long}}^{(\mathrm{j})} \sim \mathcal{N}\left(0, \sigma_{\mathrm{long}}^2\right)$ and $U_{\mathrm{eq}}^{(j)} \sim \mathcal{N}\left(0, \sigma_{\mathrm{eq}}^2\right)$, i.e., with expectation values $\langle U_{\mathrm{long}}^{(\mathrm{j})}\rangle = \langle U_{\mathrm{eq}}^{(j)}\rangle = 0$, and different standard deviations for the longitudinal and equatorial components, σ_{long} and σ_{eq}, respectively. We can combine the two contributions in Eq. (3) and write

$$\boldsymbol{\delta}_{\boldsymbol{sq}}^{(\boldsymbol{j})} = \begin{bmatrix} \Delta_{11}^{(j)} & 0 & 0 \\ 0 & \Delta_{22}^{(j)} & 0 \\ 0 & 0 & \Delta_{33}^{(j)} \end{bmatrix}, \tag{4}$$

with $\Delta_{11} \sim \mathcal{N}\left(\langle\delta_{11}\rangle, \sigma_{\mathrm{long}}^2\right)$, $\Delta_{22} \sim \mathcal{N}\left(\langle\delta_{22}\rangle, \sigma_{\mathrm{eq}}^2\right)$, and $\Delta_{33} \sim \mathcal{N}\left(\langle\delta_{33}\rangle, \sigma_{\mathrm{eq}}^2\right)$. We note that this approach is very similar as the application of an anisotropic line broadening, as it is for example known from electron paramagnetic resonance to model a distribution of spin Hamiltonian parameters.[22] Generally,

for an oblate CS-tensor shape ($\kappa \approx 1$) as expected for the square-planar Pt(II) structural motif common for all Pt sites, $\langle\delta_{11}\rangle \gg \langle\delta_{22}\rangle \approx \langle\delta_{33}\rangle$.

The individual CS-tensor components, the isotropic shift $\delta_{\mathrm{iso}}^{(j)}$, and span $\Omega^{(j)}$, and the skew $\kappa^{(j)}$, are calculated according to[23]

$$\begin{aligned} \delta_{\mathrm{iso}}^{(j)} &= \frac{1}{3}\left(\Delta'^{(j)}_{11} + \Delta'^{(j)}_{22} + \Delta'^{(j)}_{33}\right) \\ \Omega^{(j)} &= \Delta'^{(j)}_{11} - \Delta'^{(j)}_{33} \\ \kappa^{(j)} &= \frac{3\left(\Delta'^{(j)}_{22} - \delta_{\mathrm{iso}}^{(j)}\right)}{\Omega}, \end{aligned} \tag{5}$$

where the three CS-tensor components from Eq. (4) are re-assigned according to $\Delta'^{(j)}_{11} \geq \Delta'^{(j)}_{22} \geq \Delta'^{(j)}_{33}$ if required, since not necessarily $\Delta^{(j)}_{11} \geq \Delta^{(j)}_{22} \geq \Delta^{(j)}_{33}$ for each $\boldsymbol{\delta_{sq}^{(j)}}$. The marginal distribution of the random variable δ_{iso} is likewise a Gaussian distribution,

$$\delta_{\mathrm{iso}} \sim \mathcal{N}\left(\frac{1}{3}(\langle\delta_{11}\rangle + \langle\delta_{22}\rangle + \langle\delta_{33}\rangle), \frac{1}{9}\left(\sigma_{\mathrm{long}}^2 + 2\sigma_{\mathrm{eq}}^2\right)\right). \tag{6}$$

Analogously, the marginal distribution for the span can also be described by Gaussian distribution,

$$\Omega \sim \mathcal{N}\left(\langle\delta_{11}\rangle - \langle\delta_{33}\rangle, \left(\sigma_{\mathrm{long}}^2 + \sigma_{\mathrm{eq}}^2\right)\right), \tag{7}$$

however only for the case that for all $\boldsymbol{\delta_{sq}^{(j)}}$ the original assignment $\Delta^{(j)}_{11} \geq \Delta^{(j)}_{22} \geq \Delta^{(j)}_{33}$ remains valid. In the case of square-planar Pt(II), Eq. (7) is still approximately true, as long as $\Delta^{(j)}_{11} \geq \Delta^{(j)}_{22}, \Delta^{(j)}_{33}$ and $|\Omega| \gg \sigma_{\mathrm{long}}, \sigma_{\mathrm{eq}}$.

5.2 Evaluating the distribution of the CS tensors

The distribution of CS tensors $\boldsymbol{\delta_{sq}^{(j)}}$, that results from the five input parameters $\langle\delta_{11}\rangle$, $\langle\delta_{22}\rangle$,$\langle\delta_{33}\rangle$, σ_{long}, and σ_{eq}, can be conveniently evaluated by Monte-Carlo simulations. To this end, 10^7 individual CS tensors $\boldsymbol{\delta_{sq}^{(j)}}$ are constructed, and the three components $\Delta^{(j)}_{11}, \Delta^{(j)}_{22}$, and $\Delta^{(j)}_{33}$ are re-ordered into $\Delta'^{(j)}_{11} \geq \Delta'^{(j)}_{22} \geq \Delta'^{(j)}_{33}$. For each $\boldsymbol{\delta_{sq}^{(j)}}$, the three CS-tensor parameters $\delta_{\mathrm{iso}}^{(j)}$, $\Omega^{(j)}$, and $\kappa^{(j)}$ are calculated according to Eq. (5). The distribution of the CS tensors along the dimensions δ_{iso}, Ω, and κ, therefore in the following denoted as $\mathrm{P}(\delta_{\mathrm{iso}}, \Omega, \kappa) \equiv \mathrm{P}(\boldsymbol{\delta_{sq}})$, is obtained by computing a three-dimensional (3D) histogram with voxels (δ_{iso},Ω,κ ≡ $\boldsymbol{\delta_{sq}}$). Then, each voxel ($\boldsymbol{\delta_{sq}}$) represents a unique ^{195}Pt NMR signal, and its entry indicates the number of appearances (counts) of the associated CS tensor $\boldsymbol{\delta_{sq}}$ among the 10^7 individual $\boldsymbol{\delta_{sq}^{(j)}}$.

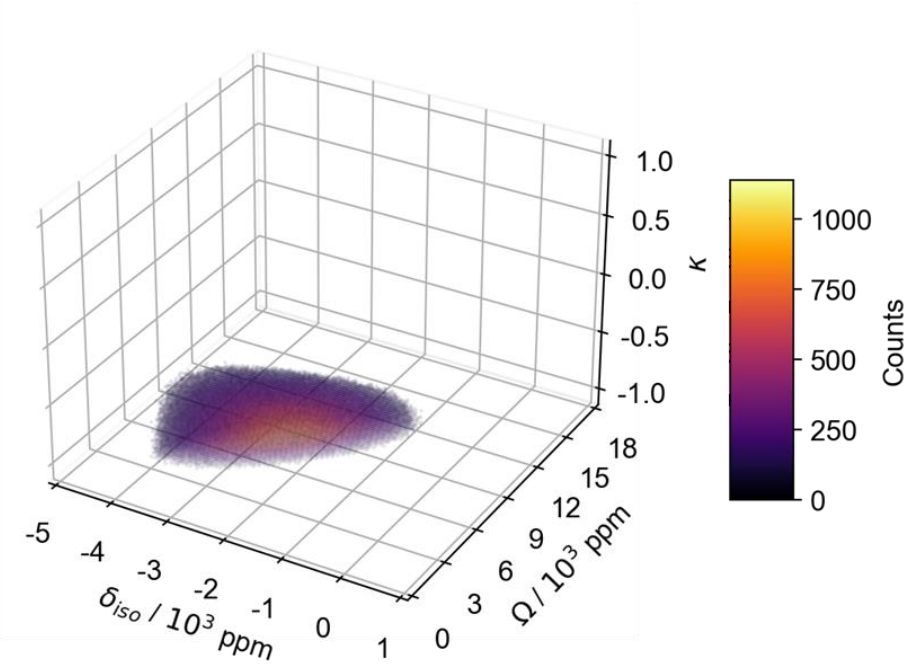

Figure S15. 3D histogram representation of the CS-tensor distribution $P(\boldsymbol{\delta_{sq}})$, with input parameters $\langle\delta_{11}\rangle = 6750$ ppm, $\langle\delta_{22}\rangle = 660$ ppm, $\langle\delta_{33}\rangle = 240$ ppm, $\sigma_{long} = 2100$ ppm, and $\sigma_{long} = 600$ ppm, resulting from the evaluation of 10^7 individual CS-tensor $\boldsymbol{\delta_{sq}^{(j)}}$. The considered parameter space was set to include $[-5000,1000]$/ppm for $\delta_{iso}^{(j)}$, $[0,18000]$/ppm for $\Omega^{(j)}$, and $[-1,1]$ for $\kappa^{(j)}$. Each dimension was equally divided into 100 bins, resulting in 10^6 voxels. A cut-off count of 10 has been included, and the color of each voxel has been rendered to be transparent to ensure comprehensibility.

This is demonstrated in **Figure S15** for the input parameters $\langle\delta_{11}\rangle = 1650$ ppm, $\langle\delta_{22}\rangle = -4440$ ppm, $\langle\delta_{33}\rangle = -4860$ ppm, $\sigma_{long} = 2100$ ppm, and $\sigma_{eq} = 600$ ppm. A more convenient graphical representation of the CS-tensor distribution $P(\boldsymbol{\delta_{sq}})$ is given by the three 2D projections, that are the three bivariate marginal distributions $P_m^{\kappa}(\delta_{iso}, \Omega)$, $P_m^{\delta_{iso}}(\Omega, \kappa)$, and $P_m^{\Omega}(\kappa, \delta_{iso})$ shown in **Figure S16**. Additionally, the respective top panels in **Figure S16** demonstrate the three marginal distributions for the isotropic chemical shift $P_m(\delta_{iso})$ in (a), for the span $P_m(\Omega)$ in (b), and for the skew $P_m(\kappa)$ in (c). We see that $P_m(\delta_{iso})$ and $P_m(\Omega)$ are indeed Gaussian distributions for the chosen input parameters, while $P_m(\kappa)$ is asymmetric. We can compute the three average CS-tensor parameters, that are here yielding $\langle\delta_{iso}\rangle = 2550$ ppm, $\langle\Omega\rangle = 6700$ ppm, and $\langle\kappa\rangle = -0.8$, respectively, indicating the center of $P(\boldsymbol{\delta_{sq}})$ in **Figure S15**, or equivalently of its marginal distributions in **Figure S16**. Note that while $\langle\delta_{iso}\rangle$ is indeed given by $\frac{1}{3}(\langle\delta_{11}\rangle + \langle\delta_{22}\rangle + \langle\delta_{33}\rangle)$, $\langle\Omega\rangle$ and $\langle\kappa\rangle$ cannot be directly calculated from $\langle\delta_{11}\rangle$, $\langle\delta_{22}\rangle$, and $\langle\delta_{33}\rangle$, due to the cases where the values of $\Delta_{11}^{(j)}$, $\Delta_{22}^{(j)}$, and $\Delta_{33}^{(j)}$ need re-ordering. $\langle\delta_{iso}\rangle$, $\langle\Omega\rangle$ and $\langle\kappa\rangle$ contain information about the average local Pt(II) environment. Information about the Pt(II)-site heterogeneity could now be obtained from the standard deviations for the three average CS-tensor parameters. However, as described in the main text, we found the marginal distribution $P_m^{\kappa}(\delta_{iso}, \Omega)$ in the δ_{iso}-Ω-space (**Figure S16**a) to be a more concise description the Pt(II)-site heterogeneity:

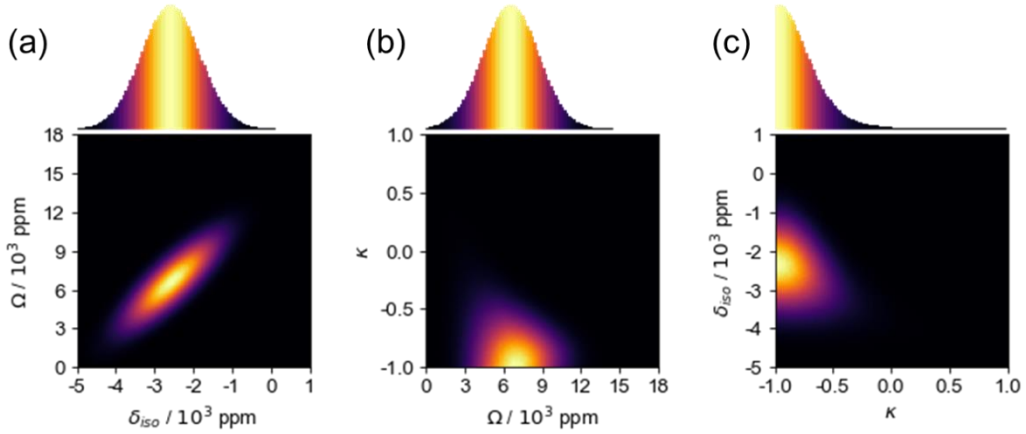

Figure S16. 2D histogram representation of the three marginal distributions (a) $P_m^{\kappa}(\delta_{iso}, \Omega)$, (b) $P_m^{\delta_{iso}}(\Omega, \kappa)$, and (c) $P_m^{\Omega}(\kappa, \delta_{iso})$, computed from the CS-tensor distribution $P(\boldsymbol{\delta_{sq}})$ shown in **Figure S15**. Accordingly, each 2D histogram comprises 10^4 pixels (see caption of **Figure S15**). The top panels show the marginal distributions of the isotropic chemical shift, $P_m(\delta_{iso})$ in (a), for the span $P_m(\Omega)$ in (b), and for the skew $P_m(\kappa)$ in (c).

for a distribution $P(\boldsymbol{\delta_{sq}})$ due to a variation of the $\Delta_{11}^{(j)}$ component only ($\sigma_{long} \gg \sigma_{eq} = 0$), all individual CS tensors $\boldsymbol{\delta_{sq}^{(j)}}$ concentrate on a line with slope $\frac{\Delta\Omega}{\Delta\delta_{iso}} = 3$ in δ_{iso}-Ω-space. This is demonstrated in **Figure S17**a for the same input parameters as described before, but $\sigma_{eq} = 0$. We can quantify this characteristic shape of $P_m^{\kappa}(\delta_{iso}, \Omega)$ by the correlation coefficient ρ of δ_{iso} and Ω, calculated from all individual $\delta_{iso}^{(j)}$ and $\Omega^{(j)}$. In the extreme case where $\sigma_{eq} = 0$, we observe a perfect correlation $\rho = 1$. For minor variation of the equatorial components $\Delta_{22}^{(j)}$ and $\Delta_{33}^{(j)}$, such that $\sigma_{long} \gg \sigma_{eq} \neq 0$, as in the example shown in **Figure S15**, the correlation is still significant with $\rho = 0.83$. This is again shown in **Figure S17**b, that corresponds to **Figure S16**a. For the other extreme case, where all components of $\boldsymbol{\delta_{sq}^{(j)}}$ vary equally, $\sigma_{long} = \sigma_{eq}$, no correlation is observed, i.e., $\rho = 0$, as shown in **Figure S17**c. Here all input parameters are again identical to those of **Figure S15**, but $\sigma_{eq} = \sigma_{long} = 4200$ ppm.

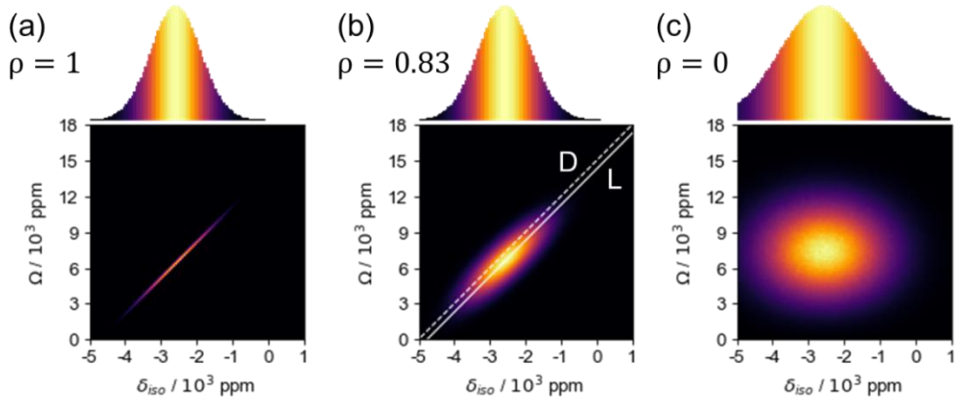

Figure S17. Marginal distributions $P_m^{\kappa}(\delta_{iso}, \Omega)$ and correlation coefficients ρ for input parameters as described for **Figure S15** (see caption), but $\sigma_{eq} = 0$ in (a), $\sigma_{eq} = 600$ ppm (identical to **Figure S15**) in (b), and $\sigma_{long} = \sigma_{eq} = 2100$ ppm in (c). In (b), the line L (solid) and the diagonal D (dashed) are explicitly indicated (see text). The marginal distributions for $P_m(\delta_{iso})$ are shown in the respective top panels The pixel size is identical to **Figure S16**. The color scale has been adjusted independently for each panel.

Before discussing further the interpretation of ρ, it is important to emphasize that computational and experimental data from this and other studies (see **Section S4**) do indeed confirm the concentration of Pt(II) environments on the line L with slope $\frac{\Delta\Omega}{\Delta\delta_{iso}} = 3$ in δ_{iso}-Ω-space. Further, different Pt(II) sites are

located at different positions along L, depending on the nature of the involved ligand atoms. For the analysis of Pt SACs, it is therefore reasonable to define the line L as the dimension of the chemical heterogeneity. The exact location of L in the δ_{iso}-Ω-space is determined by the center of $P_m^{\kappa}(\delta_{iso}, \Omega)$, and thus depends on $\langle\delta_{iso}\rangle$, $\langle\Omega\rangle$, and $\langle\kappa\rangle$. In **Figure S17**b, L is indicated by the solid white line. We can extract the distribution along L, and calculate its standard deviation, that we denote as σ in the main manuscript and use as an index for the chemical heterogeneity. To ensure comparability of σ for distributions with different locations of L, we need to define a common ppm scale. To this end, we introduce a second line D likewise with slope $\frac{\Delta\Omega}{\Delta\delta_{iso}} = 3$. The line D is initially set to run through the origin (0,0) in δ_{iso}-Ω-space, and then shifted in parallel along the direction $\frac{\Delta\Omega}{\Delta\delta_{iso}} = -\frac{1}{3}$, until D traverses either the upper or lower limit for (δ_{iso},Ω) on which $P_m^{\kappa}(\delta_{iso}, \Omega)$ is evaluated. As we have chosen the evaluation interval for Ω ([0,18000]/ppm) to be three times that of δ_{iso} ([-5000,1000]/ppm), D is the diagonal in **Figure S17**b (dashed white line), connecting (-5000,0)/ppm and (1000,18000)/ppm. We define the length of D to reflect the limits for δ_{iso}, i.e., [-5000,1000]/ppm. By projecting L on D, we can calculate σ on a globally defined ppm scale.

We note that for the special case $\rho = 1$, the marginal distributions $P_m^{\kappa}(\delta_{iso}, \Omega)$ collapse to the characteristic line L (cf. **Figure S17**a and b).

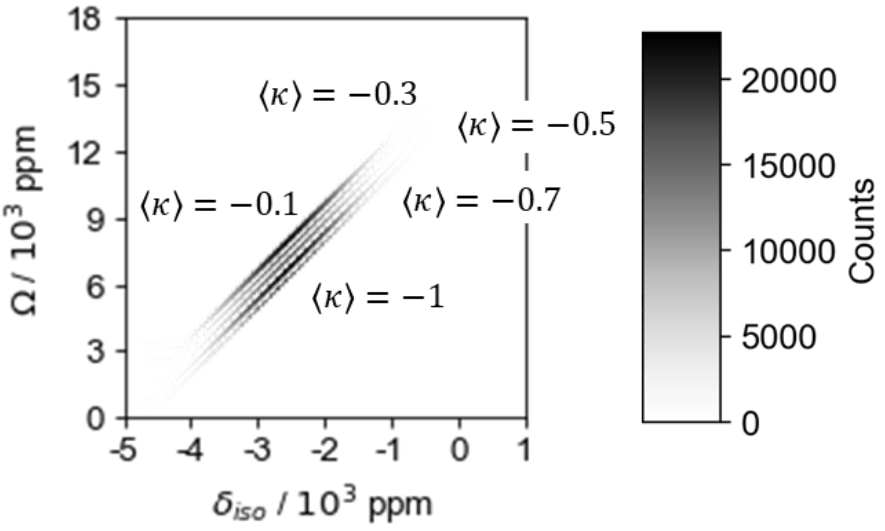

Figure S18. Marginal distributions $P_m^{\kappa}(\delta_{iso}, \Omega)$ for $\sigma_{long} = 4200$ ppm and $\sigma_{eq} = 0$, $\langle\delta_{11}\rangle = 1650$ ppm, and $\langle\delta_{22}\rangle, \langle\delta_{33}\rangle = -4650, -4650$ ppm ($\langle\kappa\rangle = -1$), $-4230, -5070$ ppm ($\langle\kappa\rangle = -0.7$), $-3810, -5490$ ppm ($\langle\kappa\rangle = -0.5$), $-3390, -5910$ ppm ($\langle\kappa\rangle = -0.3$), and $-2970, -6330$ ppm ($\langle\kappa\rangle = -0.1$). The pixel size is identical to **Figure S16**.

To further understand the interpretation of the correlation coefficient ρ, we have considered a series of marginal distributions $P_m^{\kappa}(\delta_{iso}, \Omega)$ all with for $\rho = 1$, but with different values for $\langle\kappa\rangle$. Therefore, here we set $\sigma_{long} = 4200$ ppm and $\sigma_{eq} = 0$, and also fixed $\langle\delta_{11}\rangle = 1650$ ppm. It is illustrative to now track the exact position of L for different values of $\langle\delta_{22}\rangle$ and $\langle\delta_{33}\rangle$, and thus different average skew values $\langle\kappa\rangle$. In **Figure S18**, we have shown the $P_m^{\kappa}(\delta_{iso}, \Omega)$ for $\langle\delta_{22}\rangle, \langle\delta_{33}\rangle = -4650, -4650$ ppm ($\langle\kappa\rangle = -1$), $-4230, -5070$ ppm ($\langle\kappa\rangle = -0.7$), $-3810, -5490$ ppm ($\langle\kappa\rangle = -0.5$), $-3390, -5910$ ppm ($\langle\kappa\rangle = -0.3$), and $-2970, -6330$ ppm ($\langle\kappa\rangle = -0.1$). For clarity, we have changed the color code of the count scale. Following the interpretation detailed above, each of the distributions $P_m^{\kappa}(\delta_{iso}, \Omega)$ shown in **Figure S18** represent a family of Pt(II) sites with (close-to) identical local geometry and hence $\rho = 1$,

but changing chemical environment (chemical heterogeneity only, as observed by the change in $\delta_{\mathrm{iso}}^{(j)}$). However, in the presence of several families with different average skew parameters $\langle\kappa\rangle$, we generally observe an expansion along a line perpendicular to L, i.e., a line with a slope of $\frac{\Delta\Omega}{\Delta\delta_{iso}} = -\frac{1}{3}$. Overall, the combination of all $\mathrm{P_m^{\kappa}}(\delta_{\mathrm{iso}}, \Omega)$ shown in **Figure S18** is reminiscent of the shape for $\mathrm{P_m^{\kappa}}(\delta_{\mathrm{iso}}, \Omega)$ with $\rho < 1$ (cf. **Figure S16**a). We therefore interpret the correlation coefficient as an index for the heterogeneity of the local geometry.

5.3 Numerical protocol

In order to compute the NMR signatures associated with CS-tensor distributions $\mathrm{P}(\boldsymbol{\delta_{sq}})$, as e.g., shown in **Figure S15**, in principle the individual NMR spectra associated with each voxel ($\boldsymbol{\delta_{sq}}$) can be added up, where each spectrum is weighted according to the relative voxel count. However, in the 3D histogram of $\mathrm{P}(\boldsymbol{\delta_{sq}})$ from **Figure S15**, there are 85420 populated voxels, making the computation of the overall NMR signature rather expensive. To reduce computational costs, we make use of the fact that (1) the NMR lineshape is fully defined by the span and skew (Ω,κ), while δ_{iso} only defines the center of gravity, and (2) we know that a (Gaussian) distribution of δ_{iso} produces a Gaussian broadening of the NMR line. Due to (1), all relevant NMR lineshapes associated with a given $\mathrm{P}(\boldsymbol{\delta_{sq}})$ are represented by the bivariate marginal distribution $\mathrm{P_m^{\delta_{iso}}}(\Omega, \kappa)$ shown in **Figure S16**b, comprising only 4927 populated pixels. However, to each of these pixels (Ω,κ) we need to assign a center of gravity δ_{iso}, which we can calculate from the position of the line L in the δ_{iso}-Ω-space (**Figure S16**a). Furthermore, we need to apply the correct Gaussian line broadening, which we can also extract from $\mathrm{P_m^{\kappa}}(\delta_{\mathrm{iso}}, \Omega)$. As described above, in our case for square-planar Pt(II) sites, $\mathrm{P_m^{\kappa}}(\delta_{\mathrm{iso}}, \Omega)$ is a bivariate Gaussian distribution. The conditional standard deviation σ_{con}, here referring to the standard deviation of δ_{iso} for a given $\Omega^{(j)}$, is constant and defined by

$$\sigma_{\mathrm{con}}^2 = (1-\rho)^2\sigma_{\delta_{\mathrm{iso}}}^2, \tag{8}$$

where $\sigma_{\delta_{\mathrm{iso}}}$ is the standard deviation for $\mathrm{P_m}(\delta_{\mathrm{iso}})$, and ρ is the correlation coefficient as described above. The full routine can be summarized as follows:

I. Choice of input parameters $\langle\delta_{11}\rangle$, $\langle\delta_{22}\rangle$,$\langle\delta_{33}\rangle$, σ_{long}, and σ_{eq}
II. Calculating marginal distributions $\mathrm{P_m^{\kappa}}(\delta_{\mathrm{iso}}, \Omega)$, $\mathrm{P_m^{\delta_{iso}}}(\Omega, \kappa)$, and $\mathrm{P_m}(\delta_{\mathrm{iso}})$, average CS-tensor parameters $\langle\delta_{\mathrm{iso}}\rangle$, $\langle\Omega\rangle$, and $\langle\kappa\rangle$, as well as $\mathrm{Q_{ICE}}$ parameters σ and ρ
III. Computation of the overall lineshape:
    a. The ^{195}Pt time-domain NMR signal associated with each populated pixel (Ω,κ) with $\delta_{\mathrm{iso}} = 0$ ppm is computed
    b. Each signal is scaled due to the respective relative pixel count, and multiplied with a Gaussian function to introduce a Gaussian line broadening in the frequency domain according to Eq. (8)
    c. All signals are Fourier transformed, shifted towards the correct center of gravity δ_{iso} based on the position of the line L, and added together

We note that some of these steps can be performed in either the time or frequency domain. Furthermore, for the extreme case $\rho = 0$, as e.g., shown in **Figure S17**c, the individual frequency-domain spectra do not need to be shifted according to the line L, but can all independently shifted towards $\langle\delta_{\mathrm{iso}}\rangle$. Also, then $\sigma_{\mathrm{con}} = \sigma_{\delta_{\mathrm{iso}}}$ (see Eq. (8)). Lastly, it should be noted that step IIIa has been accelerated by pre-calculating a library of ^{195}Pt time-domain NMR signals for 10^5 combination combinations (Ω,κ) using the SIMPSON simulation software.[24–28]

5.4 Comparison with other models

Well-established protocols to model the NMR lineshapes due to a distribution of nuclear sites are the Gaussian isotropic model (GIM, also cf. Czjzek model[29]), and the extended Czjzek model.[20,21] While both models have primarily been applied to describe the lineshape quadrupolar nuclei with S > ½, but has been shown to likewise applicable to the CS tensor.[20] Following this approach, the CS tensor is given by

$$\boldsymbol{\delta}^{(j)} = \boldsymbol{\delta}^{\mathbf{0}} + \lambda(\epsilon)\widetilde{\boldsymbol{\delta}}^{(j)}, \tag{9}$$

where we have used λ to denote the scaling factor to avoid confusion with the correlation coefficient ρ. The factor λ depends on the input parameter ϵ, which scales the noise contribution $\widetilde{\boldsymbol{\delta}}^{(j)}$ according to its norm,

$$\lambda(\epsilon) = \epsilon \frac{\|\boldsymbol{\delta}^{\mathbf{0}}\|}{\|\widetilde{\boldsymbol{\delta}}^{(j)}\|}, \tag{10}$$

where $\|\mathbf{A}\| = \sqrt{Tr[\mathbf{A}^2]}$ with Tr denoting the trace. The noise contribution $\widetilde{\boldsymbol{\delta}}^{(j)}$ is construct from six random variables X_{k} with $\mathrm{k} \in [1,6]$[20], that are assumed to be independent, and identically distributed according to $X_{\mathrm{k}} \sim \mathcal{N}(0,1)$ leaving four input parameters, namely the parameters $\langle\delta_{11}\rangle$, $\langle\delta_{22}\rangle$, and $\langle\delta_{33}\rangle$ to define $\boldsymbol{\delta}^{\mathbf{0}}$, and ϵ to scale the amount of noise contribution that should be considered.

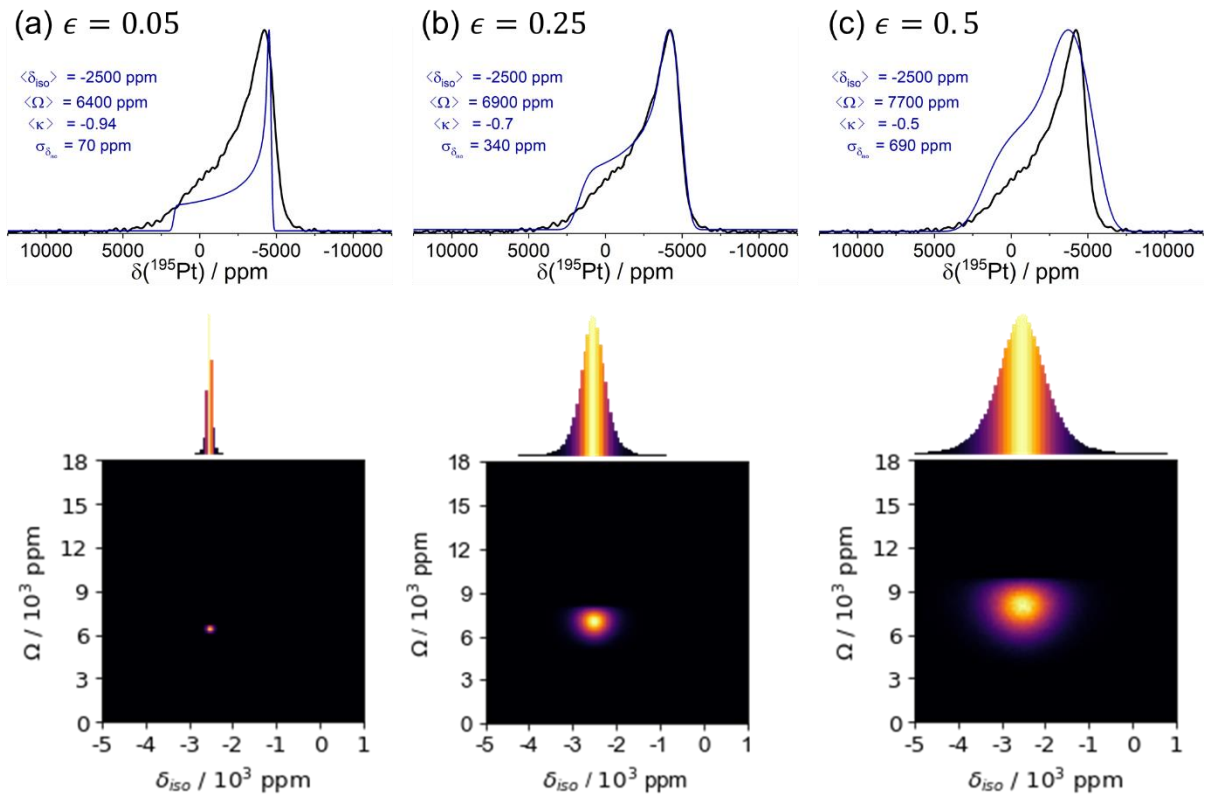

Figure S19. Comparison of the static ^{195}Pt NMR signatures for Pt@NC-15 after the second annealing with lineshapes obtained from the extended Czjzek model. In all cases, $\langle\delta_{11}\rangle = 1700$ ppm, $\langle\delta_{22}\rangle$=$\langle\delta_{33}\rangle = -4600$ ppm, with different amounts of the noise contribution $\epsilon = 0.05$ in (a), $\epsilon = 0.25$ in (b), and $\epsilon = 0.5$ in (c). Bottom panels show the corresponding marginal distributions $\mathrm{P}_{\mathrm{m}}^{\kappa}(\delta_{\mathrm{iso}}, \Omega)$ and $\mathrm{P}_{\mathrm{m}}(\delta_{\mathrm{iso}})$. The pixel size is identical to **Figure S16**. The color scale has been adjusted independently for each panel.

In **Figure S19**, we show three examples of ^{195}Pt NMR lineshapes computed according to Eq. (10), and the protocol given in **Section S5.3**. The experimental ^{195}Pt NMR signature corresponds to Pt@NC-15 after the second annealing step. For all examples, we have set $\langle\delta_{11}\rangle = 1700$ ppm, and $\langle\delta_{22}\rangle$=$\langle\delta_{33}\rangle = -4600$ ppm, and varied the varied the amount of the noise contribution $\epsilon = 0.05$ in (a), $\epsilon = 0.25$ in (b), and $\epsilon = 0.5$ in (c). The respective bottom panels show the corresponding marginal distributions $P_m^{\kappa}(\delta_{iso}, \Omega)$ in δ_{iso}-Ω-space, with the marginal distribution $P_m(\delta_{iso})$, i.e., the distribution of isotropic chemical shifts. As output parameters we report the average CS-tensor parameters, as well as the resulting width of $P_m(\delta_{iso})$, $\sigma_{\delta_{iso}}$. Clearly, none of the produced lineshape can reproduce the experimental signature well.

We note that model the noise contribution with independent, and identically distributed random variables, the δ_{iso} and Ω are of course uncorrelated ($\rho = 0$), as likewise displayed by the respective $P_m^{\kappa}(\delta_{iso}, \Omega)$. With that, **Figure S19** makes a very compelling argument for the lineshape model introduced in **Section S5.2**. From the fast MAS ^{195}Pt NMR spectrum (50 kHz ≈ 600 ppm) shown in **Figure S10**, we know that for the width of the distribution of isotropic chemical shifts, $\sigma_{\delta_{iso}} \gtrsim 600$ ppm. Without any correlation between δ_{iso} and Ω, as in the (extended) Czjzek model, this produces a broadening incompatible with the relatively narrow low-frequency part of the ^{195}Pt NMR lineshape. This is clearly demonstrated in **Figure S19**c, where $\sigma_{\delta_{iso}}$ is at the order of what would be in agreement with the fast MAS ^{195}Pt NMR spectrum. Conversely, in **Figure S19**b, where the $\sigma_{\delta_{iso}} = 340$ ppm, the broadening fits well with the low-frequency end. However, the distributions of Ω is clearly to narrow to model the continuous lineshape at the high-frequency end, again rationalizing a correlation between the CS-tensor parameters.

5.5 Robustness

In this section, we investigate the robustness of the model introduced herein towards the input parameters $\langle\delta_{11}\rangle$, $\langle\delta_{22}\rangle$,$\langle\delta_{33}\rangle$, σ_{long}, and σ_{eq}, and obtain a reasonable precision to report the output parameters $\langle\delta_{iso}\rangle$, $\langle\Omega\rangle$, $\langle\kappa\rangle$, σ, and ρ. Output parameters are in the following rounded to ppm for $\langle\delta_{iso}\rangle$, $\langle\Omega\rangle$, and σ, and to two digits for $\langle\kappa\rangle$ and ρ.

Notably, according to Eq. (6), the isotropic chemical shift δ_{iso} is always described by Gaussian distribution with standard deviation $\sigma_{\delta_{iso}} = \frac{1}{3}\sqrt{\sigma_{long}^2 + 2\sigma_{eq}^2}$. Considering the sample Pt@NC-15 after the second annealing again, which exhibits one of the largest distribution widths, this for instance gives $\sigma_{\delta_{iso}} = 755$ ppm. While $\langle\delta_{iso}\rangle$ can certainly be determined with a higher precision than $\sigma_{\delta_{iso}}$, we here make a conservative estimate and assume an uncertainty of $0.25\sigma_{\delta_{iso}} \approx 200$ ppm. In **Figure S20**a-c (left column), we show the comparison for the experimental ^{195}Pt NMR signature of Pt@NC-15 (2nd annealing), and three lineshapes with $\langle\delta_{iso}\rangle = 2350$ ppm in (a), 2550 ppm in (b), and 2750 ppm in (c). Here, (b) corresponds to the lineshape shown in the main text, with $\langle\delta_{11}\rangle = 1650$ ppm, $\langle\delta_{22}\rangle = -4440$ ppm, $\langle\delta_{33}\rangle = -4860$ ppm, $\sigma_{long} = 2100$ ppm, and $\sigma_{eq} = 600$ ppm. To obtain (a) and (c), simply $\langle\delta_{11}\rangle$, $\langle\delta_{22}\rangle$, and $\langle\delta_{33}\rangle$ have been varied in synchrony. **Figure S20**a-c confirms that uncertainty of $\langle\delta_{iso}\rangle$ can be reasonably be estimated to be within 200 ppm. Based on this and visual inspection of the experimental and simulated spectra, we have decided to report $\langle\delta_{iso}\rangle$ with a precision of 100 ppm.

As described in Eq. (7), likewise the span Ω can be approximated by a Gaussian distribution. The standard deviation, denoted as σ_Ω, can be calculated from Eq. (7), or simply from the 10^7 individual CS tensors $\boldsymbol{\delta}^{(j)}$. Again, in the case of Pt@NC-15 (2nd annealing), this gives $\sigma_\Omega = 2150$ ppm (σ_Ω =2184 ppm according to Eq. (7)). The fact that the calculated distribution width is smaller reflects the situations where $\Delta_{22}^{(j)} < \Delta_{33}^{(j)}$, which will narrow the distribution. We make the same conservative estimate as for the isotropic chemical shift, and thus assume the uncertainty for $\langle\Omega\rangle$ to be $0.25\sigma_\Omega \approx 500$ ppm.

In **FigureS20**d-f (right column), we show the comparison for the experimental ^{195}Pt NMR signature of Pt@NC-15 (2nd annealing), and three lineshapes with $\langle\Omega\rangle = 6323$ ppm in (a), 6681 ppm in (b), and 7331 ppm in (c). The input parameters were set to $\sigma_{\mathrm{long}} = 2100$ ppm, and $\sigma_{\mathrm{eq}} = 600$ ppm in all cases, and (a) $\langle\delta_{11}\rangle = 1350$ ppm, $\langle\delta_{22}\rangle = -4305$ ppm, $\langle\delta_{33}\rangle = -4695$ ppm, (b) as above, and (c) $\langle\delta_{11}\rangle = 1950$ ppm, $\langle\delta_{22}\rangle = -4575$ ppm, $\langle\delta_{33}\rangle = -5025$ ppm. $\langle\delta_{22}\rangle$ and $\langle\delta_{33}\rangle$ we varied to keep $\langle\delta_{\mathrm{iso}}\rangle = 2550$ ppm. In principle, $\langle\delta_{\mathrm{iso}}\rangle$ can be adjusted in **Figure S20**d and f to better match the high-intensity part of the spectrum. However, the lineshape remains visually worse than in (b), confirming that 500 ppm gives indeed a reasonable estimate for the uncertainty of $\langle\Omega\rangle$. Furthermore, we decided to report $\langle\Omega\rangle$ with a precision of 200 ppm.

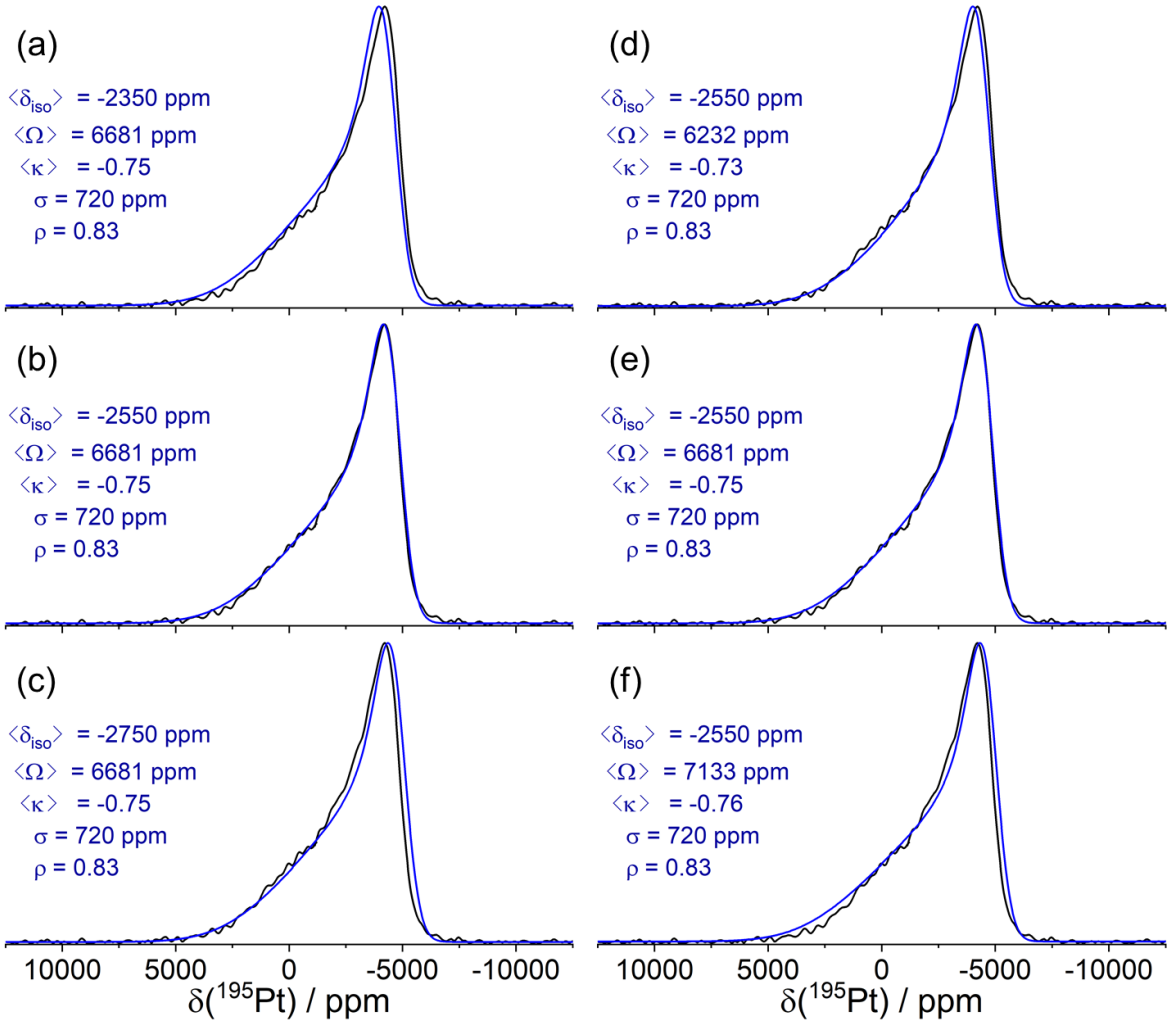

Figure S20. Evaluation for the output parameters $\langle\delta_{iso}\rangle$ in a-c, and $\langle\Omega\rangle$ in d-f. Comparison of the static ^{195}Pt NMR signatures for Pt@NC-15 after the second annealing, and lineshapes with different output parameters explicitly given in the respective panel, obtained for input parameters detailed in the text. The lineshapes have been simulated according to protocol described in **Section S5.3**.

The evaluation for the average skew $\langle\kappa\rangle$ is more complicated, since the underlying distribution for κ is typically not a Gaussian. Furthermore, the average span $\langle\Omega\rangle$ and $\langle\kappa\rangle$ are in principle not uncorrelated, but for square-planar Pt(II), where the average span values large, the effect on $\langle\kappa\rangle$ is minor (cf. **Figure S20**d-f). Then, $\langle\kappa\rangle$ mostly depends on σ_{eq}, which however crucially affects ρ. Therefore, we are left with assessing the output parameters $\langle\kappa\rangle$ and ρ simultaneously.

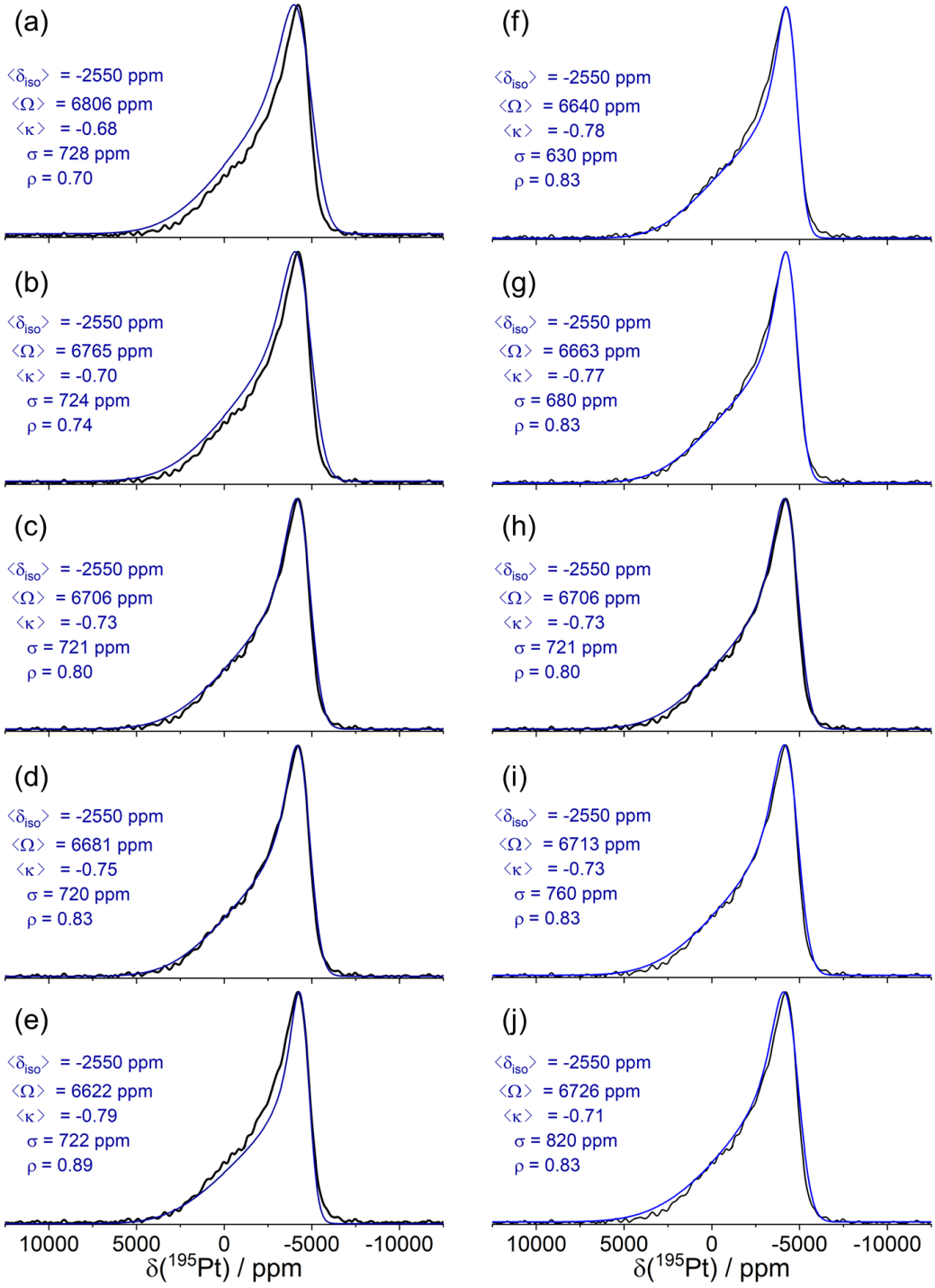

Figure S21. Evaluation for the output parameters $\langle\kappa\rangle$ and ρ in a-e, and σ in h-j. Comparison of the static ^{195}Pt NMR signatures for Pt@NC-15 after the second annealing, and lineshapes with different output parameters explicitly given in the respective panel, obtained for input parameters detailed in the text. The lineshapes have been simulated according to protocol described in **Section S5.3**.

To this end, in **Figure S21**a-e (left column), we compared to experimental ^{195}Pt NMR signature of Pt@NC-15 (2nd annealing) a series of lineshapes with $\langle\delta_{11}\rangle = 1650$ ppm, $\langle\delta_{22}\rangle = -4440$ ppm, $\langle\delta_{33}\rangle = -4860$ ppm, $\sigma_{\mathrm{long}} = 2100$ ppm, and (a) $\sigma_{\mathrm{eq}} = 840$ ppm, (b) 760 ppm, (c) 650 ppm, (d) 600 ppm, and (c) 470 ppm, where (d) again corresponds the lineshape reported in main text. We can observe how $\langle\kappa\rangle$ and ρ synchronously increase (a) $-0.68/0.7$ to (b) $-0.7/0.74$, (c) $-0.73/0.80$, (d)

$-0.75/0.83$, and (e) $-0.79/0.89$. While only minor differences are visible between the (c) and (d), a clear distinction is possible only when comparing (b) to (d) to (e). Based on this, we estimated the uncertainty for both, $\langle\kappa\rangle$ and ρ to be 0.05, and likewise reported both parameters with a precision of 0.05.

Lastly, we estimate the uncertainty for the index of the chemical heterogeneity σ. Again, σ has not a single dependence, but changes with both σ_{long} and σ_{eq}. Here, tried to keep as many other output parameters as possible constant, and calculated a series of lineshapes for $\langle\delta_{11}\rangle = 1650$ ppm, $\langle\delta_{22}\rangle = -4440$ ppm, $\langle\delta_{33}\rangle = -4860$ ppm, $\sigma_{\mathrm{long}} = 2100$ ppm, and combinations of σ_{long} and σ_{eq} that yield identical correlation coefficients ρ. A comparison with the experimental ^{195}Pt NMR signature of Pt@NC-15 (2nd annealing) is shown in **Figure S21**f-j (right column) for $\sigma_{\mathrm{long}}/\sigma_{\mathrm{eq}}$ values of (a) $1825/520$ ppm, (b) $1950/560$ ppm, (c) $2100/600$ ppm, (shown in main text), (d) $2210/630$ ppm, and (e) $2400/685$ ppm. All output parameters are explicitly given in the respective panel. σ extends from 630 ppm (a) to 820 ppm in (e), where first noticeable deviations start to become evident. Based on **Figure S21**f-j, we estimate the uncertainty for σ to be about 100 ppm. Furthermore, σ is reported with precision of 100 ppm as well.

The above model is also being implemented in the JavaScript-based web portal EasyNMR,[30] in which static spectra are calculated on the fly for all voxels of the 3D histogram in a few seconds using GPU acceleration, but for MAS spectra the approach listed above where spectra are only calculated for the 2D histogram $\mathrm{P_m^{\delta_{iso}}}(\Omega, \kappa)$. In both cases, the total spectrum is calculated in a few seconds. As an extension outside the scope of this paper, we are actively working on developing a fitting routine for the lineshape model suggested herein, to be able to further assess precisions and uncertainties, where the implementation of our model into the web portal EasyNMR[30] has been an important step towards that goal. Here we would like to emphasize, that even though uncertainties estimated in this paragraph appear high, e.g., 200 ppm for $\langle\delta_{\mathrm{iso}}\rangle$, and 500 ppm for $\langle\Omega\rangle$, they still provide meaningful information due to extreme range for e.g., $\delta_{\mathrm{iso}}/\Omega$ for the molecular compounds, extending from $-1650/-10420$ ppm for K_2PtCl_4 to $-2065/-8050$ ppm for *cis*-$Ptpy_2Cl_2$, to $-2540/-7220$ ppm for $Pt(NH_3)_4Cl_2$, to $-3840/-4600$ ppm for *cis*-$PtMe_2$tmeda.

5.6 Summary of parameters used for the studied Pt SAC samples

Table S11: Summary of the input and output parameters corresponding to the lineshapes reported in the main text.

Sample	Pt@NC-5		Pt@NC-15		Pt@NC-15	Pt@PTI
Step	1st ann	2nd ann	1st ann	2nd ann	2nd ann	2nd ann
Input						
$\langle\delta_{11}\rangle$ / ppm	4200	2800	3000	1650	1850	1600
$\langle\delta_{22}\rangle$ / ppm	-4800	-3950	-4400	-4440	-4530	-3650
$\langle\delta_{33}\rangle$ / ppm	-4800	-6150	-4900	-4860	-4970	-5750
σ_{long} / ppm	2000	1630	1020	2100	2100	2100
σ_{eq} / ppm	920	610	630	600	550	2100
Number of subspectra	5488	4621	4012	4887	5031	9502
Output	Exact values					
$\langle\delta_{iso}\rangle$ /ppm	-1800	-2100	-2100	-2550	-2550	-2600
$\langle\Omega\rangle$ / ppm	9521	7991	8138	6685	6961	7824
$\langle\kappa\rangle$	-0.78	-0.67	-0.76	-0.75	-0.77	-0.25
σ / ppm	685	541	430	727	748	1213
ρ	0.62	0.73	0.42	0.83	0.86	0
Output	Within reported precision					
$\langle\delta_{iso}\rangle$ / ppm	-1800.	-2100	-2100	-2600	-2600	-2600
$\langle\Omega\rangle$ / ppm	-9600	8000	8200	6600	7000	-7800
$\langle\kappa\rangle$	-0.80	-0.70	-0.75	-0.75	-0.75	-0.25
σ / ppm	700	500	400	700	700	1200
ρ	0.60	0.75	0.4	0.85	0.85	0

6. References

(1) Artyushkova, K. Misconceptions in Interpretation of Nitrogen Chemistry from X-Ray Photoelectron Spectra. *J. Vac. Sci. Technol. A* **2020**, *38* (3), 031002. https://doi.org/10.1116/1.5135923.

(2) Lin, R.; Kaiser, S. K.; Hauert, R.; Pérez-Ramírez, J. Descriptors for High-Performance Nitrogen-Doped Carbon Catalysts in Acetylene Hydrochlorination. *ACS Catal.* **2018**, *8* (2), 1114–1121. https://doi.org/10.1021/acscatal.7b03031.

(3) Lee, A. Y.; Blakeslee, D. M.; Powell, C. J.; John R Rumble, J. Development of the Web-Based NIST X-Ray Photoelectron Spectroscopy (XPS) Database. *Data Sci. J.* **2006**, *1* (1). https://doi.org/10.2481/dsj.1.1.

(4) Ravel, B.; Newville, M. ATHENA, ARTEMIS, HEPHAESTUS: Data Analysis for X-Ray Absorption Spectroscopy Using IFEFFIT. *J. Synchrotron Radiat.* **2005**, *12* (4), 537–541. https://doi.org/10.1107/S0909049505012719.

(5) O'Dell, L. A.; Schurko, R. W. QCPMG Using Adiabatic Pulses for Faster Acquisition of Ultra-Wideline NMR Spectra. *Chem. Phys. Lett.* **2008**, *464* (1–3), 97–102. https://doi.org/10.1016/j.cplett.2008.08.095.

(6) Koppe, J.; Bußkamp, M.; Hansen, M. R. Frequency-Swept Ultra-Wideline Magic-Angle Spinning NMR Spectroscopy. *J. Phys. Chem. A* **2021**, *125* (25), 5643–5649. https://doi.org/10.1021/acs.jpca.1c02958.

(7) Hung, I.; Gan, Z. On the Practical Aspects of Recording Wideline QCPMG NMR Spectra. *J. Magn. Reson.* **2010**, *204* (2), 256–265. https://doi.org/10.1016/j.jmr.2010.03.001.

(8) Harris, F. J. On the Use of Windows for Harmonic Analysis with the Discrete Fourier Transform. *Proc. IEEE* **1978**, *66* (1), 51–83. https://doi.org/10.1109/PROC.1978.10837.

(9) Slichter, C. P. NMR Study of Platinum Catalysts. *Surf. Sci.* **1981**, *106* (1), 382–396. https://doi.org/10.1016/0039-6028(81)90226-0.

(10) Rhodes, H. E.; Wang, P.-K.; Makowka, C. D.; Rudaz, S. L.; Stokes, H. T.; Slichter, C. P.; Sinfelt, J. H. NMR of Platinum Catalysts. II. Relaxation. *Phys. Rev. B* **1982**, *26* (7), 3569–3574. https://doi.org/10.1103/PhysRevB.26.3569.

(11) Rhodes, H. E.; Wang, P.-K.; Stokes, H. T.; Slichter, C. P.; Sinfelt, J. H. NMR of Platinum Catalysts. I. Line Shapes. *Phys. Rev. B* **1982**, *26* (7), 3559–3568. https://doi.org/10.1103/PhysRevB.26.3559.

(12) Ansermet, J.-Ph.; Slichter, C. P.; Sinfelt, J. H. Solid State NMR Techniques for the Study of Surface Phenomena. *Prog. Nucl. Magn. Reson. Spectrosc.* **1990**, *22* (5), 401–421. https://doi.org/10.1016/0079-6565(90)80005-3.

(13) te Velde, G.; Bickelhaupt, F. M.; Baerends, E. J.; Fonseca Guerra, C.; van Gisbergen, S. J. A.; Snijders, J. G.; Ziegler, T. Chemistry with ADF. *J. Comput. Chem.* **2001**, *22* (9), 931–967. https://doi.org/10.1002/jcc.1056.

(14) Autschbach, J. The Role of the Exchange-Correlation Response Kernel and Scaling Corrections in Relativistic Density Functional Nuclear Magnetic Shielding Calculations with the Zeroth-Order Regular Approximation. *Mol. Phys.* **2013**, *111* (16–17), 2544–2554. https://doi.org/10.1080/00268976.2013.796415.

(15) van Lenthe, E.; Snijders, J. G.; Baerends, E. J. The Zero-order Regular Approximation for Relativistic Effects: The Effect of Spin–Orbit Coupling in Closed Shell Molecules. *J. Chem. Phys.* **1996**, *105* (15), 6505–6516. https://doi.org/10.1063/1.472460.

(16) van Lenthe, E.; van Leeuwen, R.; Baerends, E. J.; Snijders, J. G. Relativistic regular two-component Hamiltonians. *Int. J. Quantum Chem.* **1996**, *57* (3), 281–293. https://doi.org/10.1002/(SICI)1097-461X(1996)57:3<281::AID-QUA2>3.0.CO;2-U.

(17) Venkatesh, A.; Gioffrè, D.; Atterberry, B. A.; Rochlitz, L.; Carnahan, S. L.; Wang, Z.; Menzildjian, G.; Lesage, A.; Copéret, C.; Rossini, A. J. Molecular and Electronic Structure of Isolated Platinum Sites Enabled by the Expedient Measurement of 195Pt Chemical Shift Anisotropy. *J. Am. Chem. Soc.* **2022**, *144* (30), 13511–13525. https://doi.org/10.1021/jacs.2c02300.

(18) Wang, Z.; Völker, L. A.; Robinson, T. C.; Kaeffer, N.; Menzildjian, G.; Jabbour, R.; Venkatesh, A.; Gajan, D.; Rossini, A. J.; Copéret, C.; Lesage, A. Speciation and Structures in Pt Surface

Sites Stabilized by N-Heterocyclic Carbene Ligands Revealed by Dynamic Nuclear Polarization Enhanced Indirectly Detected 195Pt NMR Spectroscopic Signatures and Fingerprint Analysis. *J. Am. Chem. Soc.* **2022**, *144* (47), 21530–21543. https://doi.org/10.1021/jacs.2c08300.

(19) Lucier, B. E. G.; Reidel, A. R.; Schurko, R. W. Multinuclear Solid-State NMR of Square-Planar Platinum Complexes — Cisplatin and Related Systems. *Can. J. Chem.* **2011**, *89* (7), 919–937. https://doi.org/10.1139/v11-033.

(20) Vasconcelos, F.; Cristol, S.; Paul, J.-F.; Delevoye, L.; Mauri, F.; Charpentier, T.; Caër, G. L. Extended Czjzek Model Applied to NMR Parameter Distributions in Sodium Metaphosphate Glass. *J. Phys. Condens. Matter* **2013**, *25* (25), 255402. https://doi.org/10.1088/0953-8984/25/25/255402.

(21) Caër, G. L.; Bureau, B.; Massiot, D. An Extension of the Czjzek Model for the Distributions of Electric Field Gradients in Disordered Solids and an Application to NMR Spectra of 71Ga in Chalcogenide Glasses. *J. Phys. Condens. Matter* **2010**, *22* (6), 065402. https://doi.org/10.1088/0953-8984/22/6/065402.

(22) Shaltiel, D.; Low, W. Anisotropic Broadening of Linewidth in the Paramagnetic Resonance Spectra of Magnetically Dilute Crystals. *Phys. Rev.* **1961**, *124* (4), 1062–1067. https://doi.org/10.1103/PhysRev.124.1062.

(23) Herzfeld, J.; Berger, A. E. Sideband Intensities in NMR Spectra of Samples Spinning at the Magic Angle. *J. Chem. Phys.* **1980**, *73* (12), 6021–6030. https://doi.org/10.1063/1.440136.

(24) Bak, M.; Rasmussen, J. T.; Nielsen, N. C. SIMPSON: A General Simulation Program for Solid-State NMR Spectroscopy. *J. Magn. Reson.* **2000**, *147* (2), 296–330. https://doi.org/10.1006/jmre.2000.2179.

(25) Vosegaard, T.; Malmendal, A.; Nielsen, N. C. The Flexibility of SIMPSON and SIMMOL for Numerical Simulations in Solid-and Liquid-State NMR Spectroscopy. *Monatshefte Für Chem. Chem. Mon.* **2002**, *133* (12), 1555–1574. https://doi.org/10.1007/s00706-002-0519-2.

(26) Tošner, Z.; Vosegaard, T.; Kehlet, C.; Khaneja, N.; Glaser, S. J.; Nielsen, N. Chr. Optimal Control in NMR Spectroscopy: Numerical Implementation in SIMPSON. *J. Magn. Reson.* **2009**, *197* (2), 120–134. https://doi.org/10.1016/j.jmr.2008.11.020.

(27) Bak, M.; Rasmussen, J. T.; Nielsen, N. Chr. SIMPSON – An Important Driver for Numerical Simulations in Solid-State NMR Spectroscopy. *J. Magn. Reson.* **2011**, *213* (2), 401–403. https://doi.org/10.1016/j.jmr.2011.08.002.

(28) Tošner, Z.; Andersen, R.; Stevensson, B.; Edén, M.; Nielsen, N. Chr.; Vosegaard, T. Computer-Intensive Simulation of Solid-State NMR Experiments Using SIMPSON. *J. Magn. Reson.* **2014**, *246*, 79–93. https://doi.org/10.1016/j.jmr.2014.07.002.

(29) Czjzek, G.; Fink, J.; Götz, F.; Schmidt, H.; Coey, J. M. D.; Rebouillat, J.-P.; Liénard, A. Atomic Coordination and the Distribution of Electric Field Gradients in Amorphous Solids. *Phys. Rev. B* **1981**, *23* (6), 2513–2530. https://doi.org/10.1103/PhysRevB.23.2513.

(30) Juhl, D. W.; Tošner, Z.; Vosegaard, T. Chapter One - Versatile NMR Simulations Using SIMPSON. In *Annual Reports on NMR Spectroscopy*; Webb, G. A., Ed.; Academic Press, 2020; Vol. 100, pp 1–59. https://doi.org/10.1016/bs.arnmr.2019.12.001.